Research Article | Vol. 10, No. 11 / 1 November 2019 / Biomedical Optics Express 5877
Biomedical Optics EXPRESS

Spatial localization of mechanical excitation affects spatial resolution, contrast, and contrast-to-noise ratio in acoustic radiation force optical coherence elastography

NICHALUK LEARTPRAPUN,[1] RISHYASHRING R. IYER,[1,2] COLIN D. MACKEY,[1] AND STEVEN G. ADIE[1,*]

[1]Cornell University, Meinig School of Biomedical Engineering, Weill Hall, Ithaca, New York 14853, USA
[2]Present address: University of Illinois at Urbana-Champaign, Beckman Institute for Advanced Science and Technology, Urbana, Illinois 61801, USA
[*]sga42@cornell.edu

Abstract: The notion that a spatially confined mechanical excitation would produce an elastogram with high spatial resolution has motivated the development of various elastography techniques with localized mechanical excitation. However, a quantitative investigation of the effects of spatial localization of mechanical excitation on the spatial resolution of elastograms is still lacking in optical coherence elastography (OCE). Here, we experimentally investigated the effect of spatial localization of acoustic radiation force (ARF) excitation on spatial resolution, contrast, and contrast-to-noise ratio (CNR) of dynamic uniaxial strain elastograms in dynamic ARF-OCE, based on a framework for analyzing the factors that influence the quality of the elastogram at different stages of the elastography workflow. Our results show that localized ARF excitation with a smaller acoustic focal spot size produced a strain elastogram with superior spatial resolution, contrast, and CNR. Our results also suggest that the spatial extent spanned by the displacement response in the sample may connect between the spatial localization of the mechanical excitation and the resulting elastogram quality. The elastography framework and experimental approach presented here may provide a basis for the quantitative analysis of elastogram quality in OCE that can be adapted and applied to different OCE systems and applications.

1. Introduction

Biomechanical interactions between cells and their surroundings play an important role in both physiological and pathological processes across a wide range of length scales [1–4]. At the organ level, clinical elastography techniques have enabled diagnostics of diseases such as liver fibrosis, breast cancer, and multiple sclerosis via the altered mechanical properties of pathological tissues [5,6]. At the cellular to tissue levels, emerging optical elastography techniques and nano- to micro-scale mechanical characterization methods such as atomic force microscopy (AFM) and microrheology [7–9] are finding applications in the study of cell mechanics and the field of mechanobiology. Among others, optical coherence elastography (OCE) is capable of probing mechanical properties of both biological tissues and engineered biological systems at the micrometer-to-millimeter scales [10–12]. At these length scales, the pursuit of higher spatial resolution elastogram is one of the motivating factors for the development of novel elastography approaches [13–16].

A conjecture exists in the field of elastography that in order to probe spatial variation in mechanical properties with high spatial resolution, the externally applied stress field must be confined to a very small region in 3-dimensional (3D) space [17–19]. In other words, in order to measure the local mechanical properties of a sample with minimal confounding contributions

#374995 https://doi.org/10.1364/BOE.10.005877
Journal © 2019 Received 8 Aug 2019; revised 30 Sep 2019; accepted 6 Oct 2019; published 24 Oct 2019

Biomedical Optics EXPRESS

from the distribution of mechanical properties in the neighboring regions, one must apply spatially localized mechanical excitation that generates spatially localized displacement field in the sample [20]. It has been proposed that such spatial localization would lead to the displacements measured at the point of excitation being highly correlated to the local mechanical properties of the sample at that location [20]. Furthermore, the ability to resolve microscopic mechanical properties in nano- or micro-indentation testing with AFM has also been attributed to the applied stress that is highly localized in 3D space underneath the indenter tip [21–24]. This has motivated the development of numerous elastography techniques with localized mechanical excitation over the past two decades, including acousto-vibrography [17], acoustic radiation force impulse imaging (ARFI) [18,20], as well as various implementations of OCE [14,24–28]. However, the notion that a more spatially localized mechanical excitation would improve the spatial resolution of the elastogram remains relatively under-investigated, both theoretically and experimentally, despite having had a significant influence on the field of elastography.

We present an experimental investigation of the effect of spatial localization of mechanical excitation on spatial resolution, contrast, and contrast-to-noise ratio (CNR) of the obtained strain elastogram in dynamic acoustic radiation force optical coherence elastography (ARF-OCE). Expanding upon our previous experiments characterizing spatial resolution in ARF-OCE [29] and the framework for analyzing spatial resolution in compression OCE recently proposed by Hepburn et al. [30], we discuss the factors that contribute to the final elastogram quality at different stages of the elastography workflow. Our modified framework takes into account the region of excitation (ROE), a measure of the spatial localization of the applied mechanical excitation, and the region of response (ROR), a measure of the spatial range of the induced displacement response in the sample. We experimentally characterized ROR and the resulting elastogram quality as a function of ARF excitation ROE, modulation frequency, and sample mechanical properties. Lastly, we analyzed the correlation between the measured ROR and the elastogram quality to investigate the hypothesis that a spatially confined mechanical excitation improves spatial resolution of the elastogram via spatial localization of the sample displacement response.

2. Framework for analyzing factors influencing elastogram quality

The spatial resolution of an OCE system has typically been loosely defined based on the spatial resolution of its parent imaging modality, optical coherence tomography (OCT), or the known limits imposed by the elastogram reconstruction process [31–33]. However, the concept of spatial resolution in elastography cannot be treated as an independent system parameter in the same way that spatial resolution can be defined for a given imaging system. Recently, a framework has been proposed for analyzing the spatial resolution of strain elastogram in quasi-static compression OCE that, for the first time, explicitly accounts for the contributions of not only the OCT system resolution and the elastogram reconstruction process, but also the mechanical deformation in the sample [30]. We expand upon this proposed framework to identify additional factors that influence the elastogram quality at different stages of the elastography workflow for any general elastography system (Fig. 1). Our expanded framework distinguishes the physical response of the sample to the applied mechanical excitation from the measured response that depends on the OCE system specification and post-processing algorithms. Together with the applied mechanical excitation, the image acquisition and data processing to obtain the measured response from the physical response of the sample constitute the elastography system, whose output is the final elastogram. We discuss the different elements of an elastography system in the following sub-sections. We note that these elements are present in any general elastography system, but the specific factors and metrics (examples of which are provided in Fig. 1) that influence and characterize their performance may be tailored to each specific system.

Biomedical Optics EXPRESS

2.1. Mechanical excitation

Mechanical excitation is the first step in any elastography measurement. It is the input to the elastography system that induces a measurable displacement response in the sample. The type of mechanical excitation is typically classified by its temporal (e.g., quasi-static [30–32] versus dynamic [25–27,34], transient [15,35,36] versus continuous [14,37]) and spatial (e.g. bulk [31,32] versus localized [14,28,38], uniform [39] versus varying [25,37,40]) characteristics. Spatially localized excitation can be characterized by its ROE, which is a measure of the spatial domain over which stress field is applied to the sample. For a given temporal and spatial profiles, the magnitude of excitation determines the regime (e.g. linear versus nonlinear) in which the measurements take place. Characteristics of the mechanical excitation not only affects the response in the sample, but also often informs the types of image acquisition and data processing that are implemented to obtain the final elastogram. In this paper, continuous harmonic ARF excitation is implemented with both wide-area uniform excitation and localized excitation.

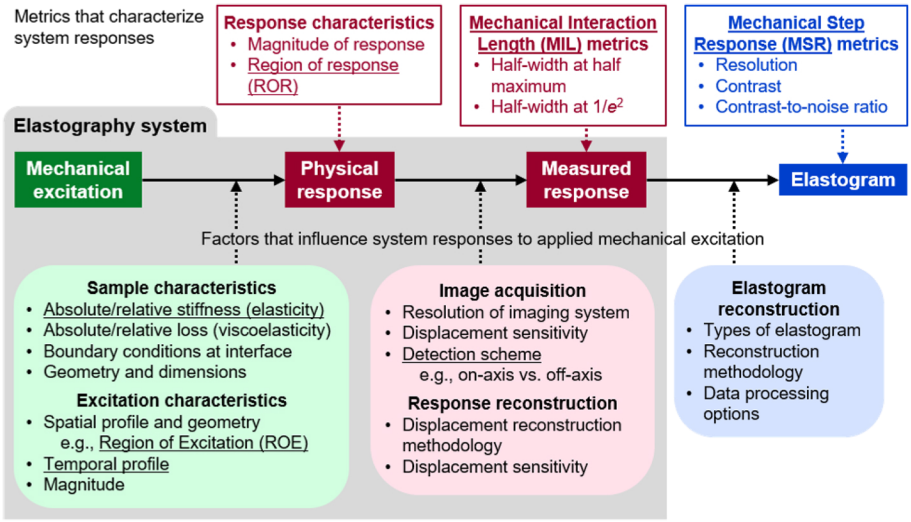

Fig. 1. Flowchart of a general elastography workflow illustrating factors that contribute to the quality of the final elastogram and parameters that characterize the system response at different stages. Factors that are investigated in this paper are underlined.

2.2. Physical response

The applied mechanical excitation induces a physical response in the sample. The physical response is a result of work done by the applied mechanical excitation (i.e., applied force). The portion of the work done that is converted to strain energy stored in the sample gives rise to the sample deformation. The physical response is dependent on the characteristics of both the mechanical excitation and the sample itself. The characteristics of the sample may be described by its mechanical properties, geometry, and boundary conditions. For a sample with mechanical inhomogeneity, both the absolute mechanical properties in each region and the relative mechanical properties between regions in the sample affect the physical response. In addition, the boundary conditions at the interfaces between regions of mechanical inhomogeneity must also be considered. For instance, mechanically bounded interfaces between a tumor and surrounding stromal tissues may be described with a non-slip displacement boundary condition. On the other hand, unbounded interfaces between two interstitial tissue compartments may be

Biomedical Optics EXPRESS

described with a traction boundary condition representing the frictional interaction with the interstitial fluid.

2.3. Measured response

The only practically accessible response from the elastography system is the measured displacement response, which is a representation of the physical response of the sample as perceived by the image acquisition and subsequent data processing steps. The measured response in OCE is typically the component of the sample displacement parallel to the direction of the axially applied excitation. How closely the measured response correlates to the physical response depends on both the performance of the imaging system (e.g., spatial resolution, sensitivity, etc.) and the detection scheme, as well as the reconstruction of the sample displacement from the acquired image data. In the framework proposed by Hepburn et al., these factors together contribute to the OCE system resolution [30].

The on-axis detection scheme only measures the local sample displacement at the point of excitation, whereas the off-axis detection scheme measures the displacement field in the sample induced by the excitation. The former is implemented in bulk compression OCE [13,30–32] as well as some localized-excitation OCE such as magnetomotive OCE [38], photonic force OCE [14], and nanobomb OCE [28]. The latter is implemented in quantitative shear wave elastography techniques [35,37,40]. The accuracy and precision of the sample displacement measurement is limited by the displacement sensitivity of the imaging system and any limits imposed by the displacement reconstruction process (e.g., spatial averaging). In OCE, sample displacement is typically measured in the axial direction, parallel to the OCT detection beam, in order to leverage the sub-nanometer displacement sensitivity of phase-sensitive OCT [41].

2.4. Elastogram

The elastogram is the final output of the elastography system. It is the outcome of data processing procedures performed on the measured response to reconstruct the output parameter that bears the most resemblance to the spatial distribution of mechanical properties in the sample. For techniques that utilize on-axis detection scheme, uniaxial strain is typically computed from the sample displacement field. Under the assumption of linearity, and that the applied stress is uniform and uniaxial, the reconstructed uniaxial local strain is inversely proportional to the local Young's modulus of the sample [30–32]. Attempts to account for transverse stress variation have been made by incorporating a stress sensor that allows the Young's modulus of the sample to be obtained directly from the measured uniaxial local stress and strain [13,42]. On the other hand, off-axis elastography techniques typically reconstruct shear modulus directly from the measured shear wave displacement field by calculating the shear wave speed and assuming either elasticity or a rheological model [35]. Some approaches have eliminated the need for a rheological model assumption by leveraging both the propagation speed and attenuation of the measured shear wave displacement field [37,40]. The quality of the elastogram, including spatial resolution, is highly dependent on the type of the elastogram that is reconstructed, as well as any contributions from data processing in the reconstruction process. In this paper, uniaxial strain elastograms are reconstructed from the measured dynamic axial sample displacement response.

3. Metrics for characterizing responses of elastography system

In order to investigate the contributions of factors affecting the quality of the final elastogram, quantifiable metrics are needed to characterize the system responses at different stages of the elastography workflow (Fig. 1). The investigation in this paper is specifically concerned with the effect of ROE on the elastogram quality, which may be connected via the ROR that results from the spatially confined mechanical excitation. Mechanical interaction length (MIL), which can be quantified from the measured response, is proposed as a quantitative measure of the ROR

Biomedical Optics EXPRESS

(Fig. 2(a)). The quality of the resulting elastogram is quantified based on image performance metrics derived from mechanical step response (MSR) (Fig. 2(b)).

3.1. Mechanical interaction length

MIL provides a quantitative measure for ROR (spatial extent of the displacement field in 3D space resulting from mechanical excitation). MIL represents the spatial range about the point of excitation over which the applied mechanical excitation can induce a certain level of physical response in the sample. In other words, it represents the distance from the point of excitation to a location in the sample that can "mechanically interact" with the point of excitation. In this paper, we compute MIL along the transverse direction, although in principle it could be computed along any axis in 3D space that intersects the location of the applied mechanical excitation. It follows that the physical resp xc lu ion of mechanical proper hi at t, it may imply that any m eit ra OR r ved based on the measur ro t, a l he point of excitation if the c n (thermal) such t echanical excitation due to t l that location is physically r be measured for as far as it r MIL is e to its p ching t -width a izes the sample deformation c d, half-width at $1/e^2$ of the r e displacement field caused secondarily by the induced mechanical wave propagating away from the point of excitation. The distinction between the two MIL metrics will be further explored in Sections 5 and 6.

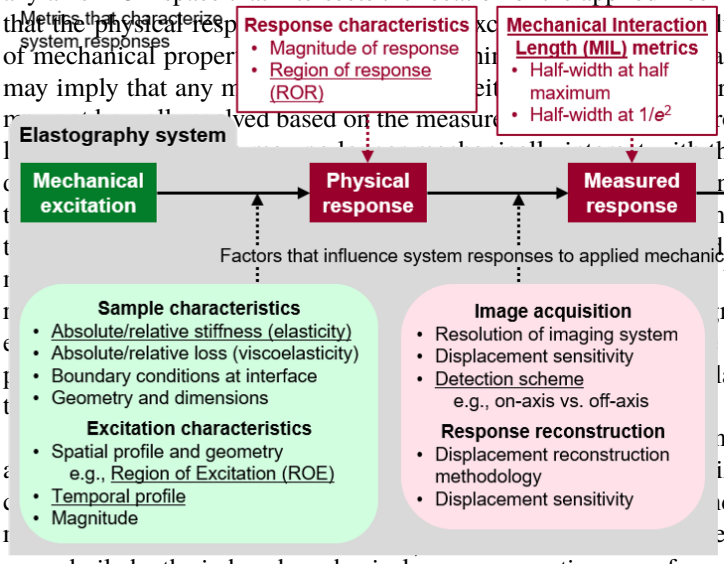

Fig. 1.

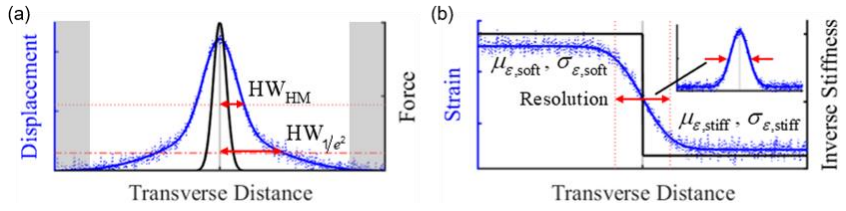

Fig. 2.

Fig. 2. Illustrations of MIL and MSR to characterize the sample response to localized mechanical excitation. (a) MIL is measured from the sample displacement response (blue) induced by localized ARF excitation (black). Red double-headed arrows indicate the MIL metrics: half-width at half-maximum displacement, HW_{HM}, and half-width at $1/e^2$ of the maximum displacement, HW_{1/e^2}. Shaded areas e sent locations where the sample is no longer considered to be mechanical h the point of excitation. (b) MSR is measured from the reconstructed uni gram (blue) of a sample containing a sharp step variation in mechanical pr Red double-headed arrow indicates spatial resolution; inset illustrates equiva onse of the reconstructed step response with red arrows denoting the spatial $\mu_{\varepsilon,soft}$, $\mu_{\varepsilon,stiff}$, $\sigma_{\varepsilon,soft}$, and $\sigma_{\varepsilon,stiff}$ denote median and standard deviation of uniaxial strain measured on the soft and stiff sides, respectively.

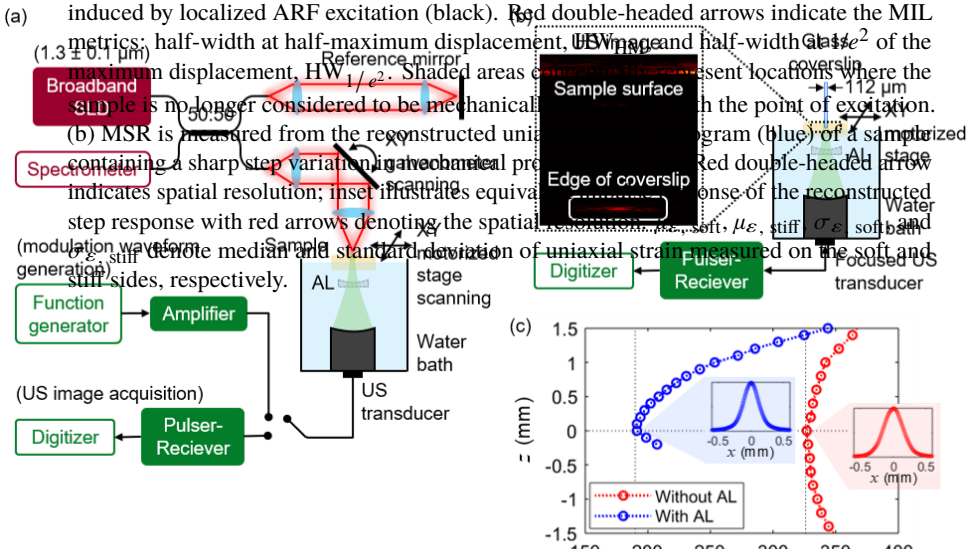

Biomedical Optics EXPRESS

3.2. Mechanical step response and performance metrics of elastogram

MSR is a measure of how well the elastogram captures the presence of a sharp mechanical step (i.e., variation in mechanical properties resembling a Heaviside step function) in the sample. MSR represents the ability to reveal the existence of mechanical inhomogeneity in the sample from the obtained elastogram, which involves both spatially resolving mechanically heterogeneous structures and detecting differences in the mechanical properties in the sample. Three MSR metrics are defined from the reconstructed uniaxial strain elastogram (Fig. 2(b)), adapted from image quality metrics commonly used in ultrasound elastography [44].

Spatial resolution characterizes the ability to spatially resolve regions in the sample with different mechanical properties on the elastogram. Spatial resolution is defined as the full width at half-maximum (FWHM) of the equivalent impulse response (i.e., derivative of the reconstructed uniaxial strain amplitude w.r.t. spatial coordinate across the mechanical step). This definition is analogous to measuring the FWHM of a Gaussian point spread function of a sub-resolution target in optical imaging. Contrast and contrast-to-noise ratio (CNR) characterize the ability to perceive differences in the elastogram that are due to the mechanical properties within the sample. Resolution, contrast and CNR are given by the expressions:

$$\text{Resolution} = \left(2\sqrt{\ln 2}\right) w, \tag{1}$$

$$\text{Contrast} = \frac{\mu_{\varepsilon,\,\text{soft}} - \mu_{\varepsilon,\,\text{stiff}}}{\mu_{\varepsilon,\,\text{soft}} + \mu_{\varepsilon,\,\text{stiff}}}, \tag{2}$$

$$\text{CNR} = \frac{\mu_{\varepsilon,\,\text{soft}} - \mu_{\varepsilon,\,\text{stiff}}}{\sqrt{\sigma^2_{\varepsilon,\,\text{soft}} + \sigma^2_{\varepsilon,\,\text{stiff}}}}, \tag{3}$$

where w denotes the $1/e$ radius of a Gaussian impulse response, while μ_ε and σ_ε denote the median and standard deviation of the reconstructed uniaxial strain amplitude on each side of the mechanical step (subscripts indicate softer or stiffer side), respectively. We note that other definitions exist for mechanical contrast and CNR [45–47]. Here, we adopt the definitions based on the median and standard deviation of the strain responses on each side for characterizing the MSR between two mechanically homogeneous regions. In addition, we note that strain contrast by itself may not necessarily be a complete indicator of the actual distribution of elastic moduli in the sample due to the possibility of non-uniform stress distribution that is unaccounted for.

4. Methods

4.1. Experimental setup

The experimental setup consisted of a custom-built ARF-OCE system and an ultrasound imaging subsystem for measuring the acoustic beam profile for ARF excitation.

4.1.1. Acoustic radiation force optical coherence elastography system

The ARF-OCE system consisted of a spectral-domain (SD) OCT setup for imaging the sample displacement response, where the OCT beam interrogated the sample from the top, and an ultrasonic (US) transducer for applying ARF excitation, where the acoustic beam entered the sample from below (Fig. 3(a)). The two counter-propagating OCT and US beams were initially co-axially aligned at the center of the field-of-view (FOV). The SD-OCT system utilized a broadband superluminescent diode (Thorlabs, LS2000B) source with a center wavelength of 1300 nm and a bandwidth of 200 nm, a 2-axis galvanometer for beam-scanning, and a spectrometer (Cobra 1300, Wasatch Photonics) with a bandwidth of 245 nm and a line-scan camera (GL2048, Sensors Unlimited) with 2048 pixels for acquisition. The axial and transverse resolutions of the OCT system were 3.7 μm and 6 μm in air, respectively. The axial displacement noise floor was

Biomedical Optics EXPRESS

in the range of 0.6-1.5 nm, depending on the modulation frequency and OCT signal-to-noise ratio (SNR). The sample was mounted on a 2-axis motorized stage. The galvanometer and the motorized stage were alternatively used for the off-axis and the on-axis detection schemes, respectively. A function generator supplied voltage-controlled modulation waveform to the US transducer via a power amplifier for the harmonic ARF excitation. Instrument controls and synchronizations were performed via data acquisition cards according to a custom acquisition software written in LabVIEW.

4.1.2. Acoustic radiation force excitation and ultrasound imaging subsystem

Two water-immersion US transducers with a carrier frequency of 10 MHz were alternatively used for either wide-area or localized ARF excitation. The former was achieved by an unfocused US transducer (Olympus, V312-SU) with an element size of 6 mm in diameter. The latter was achieved by a focused US transducer (Olympus, V322-SU) with an element size of 25.4 mm in diameter and a nominal focal length of 51 mm. In addition to the native focusing of this transducer, a custom-made acoustic lens (AL) was placed inside the water bath, between the focused US transducer and the sample, to further focus the acoustic beam to a smaller focal spot for investigating the effect of ROE. The AL was a concave lens made of a resin material (Epoxy Technology, EPO-TEK 301) with a radius of curvature of 25.4 mm. Acoustic impedance and speed of sound in the AL material were 3.05 MPa·s·mm^{-1} and 2650 m·s^{-1}, respectively [48]. Single-pass acoustic transmissivity through the AL in water was 0.67.

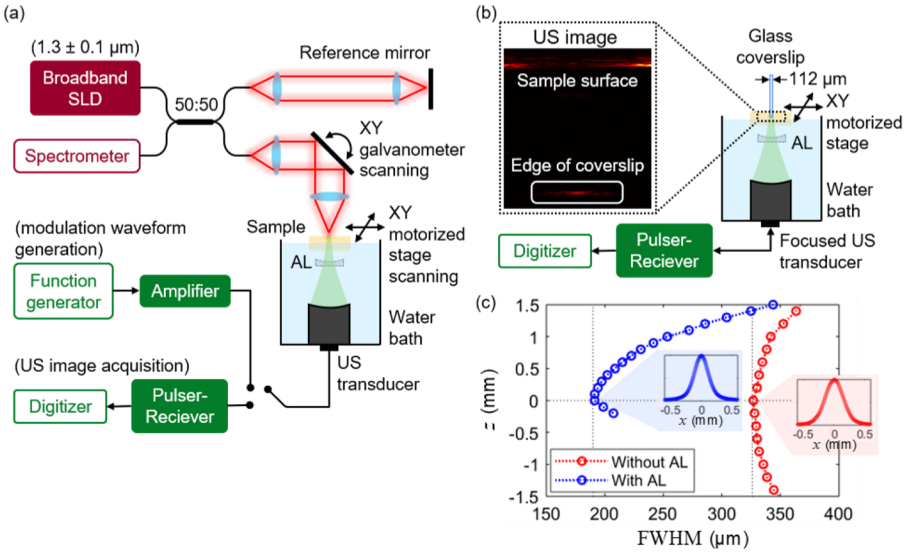

Fig. 3. ARF-OCE system. (a) Schematic of ARF-OCE system. An SD-OCT system with a 1300-nm center wavelength broadband SLD source, interrogated the sample from the top to measure the sample displacement. A water-immersion US transducer provided ARF excitation from below the sample. (b) Schematic of acoustic beam profile measurement setup, using the edge of a glass coverslip as a sub-resolution line target. An example B-mode US image of the coverslip edge is shown. (c) FWHM of acoustic LSF as a function of axial position for native focusing (red) and additional AL focusing (blue). Insets show LSF as a function of lateral position, x, at the focal plane for each case. The axial position, z, is defined w.r.t. the acoustic focal plane. SLD: superluminescent diode, US: ultrasonic, AL: acoustic lens.

Biomedical Optics EXPRESS

A custom-built US imaging subsystem (Fig. 3(b)) was used to measure the ROE for the two localized excitation schemes (with and without AL), where the ROE is defined as the FWHM of the acoustic focal spot size in each case. The acoustic beam profile was obtained by imaging the edge of a 112-µm thick glass coverslip that was vertically embedded in a 1% agar gel; the cross-section of the bottom edge of the coverslip was used as a sub-resolution line target for the acoustic beam. The US imaging subsystem consisted of a pulser-receiver (Olympus, 5073PR) for transmitting and receiving US pulses and a high-speed digitizer (Alazar Technologies, ATS9360-101) for data acquisition. Cross-sectional B-mode US image of the coverslip edge was acquired by translating the sample laterally on the motorized stage. The line spread function (LSF) of the acoustic beam as a function of depth was obtained by repeatedly acquiring a B-mode image after manually translating the sample to a different axial position. The increase in numerical aperture of the beam with additional focusing by the AL is evident in the profile of FWHM of LSF as a function of depth (Fig. 3(c)). The acoustic focal spot sizes with and without the AL were 190 µm and 326 µm, respectively. We note that for an acoustic beam with a smaller expected focal spot size, a narrower line target than the coverslip used here may be needed for accurate LSF measurements.

In summary, three levels of spatial localization of the ARF excitation were achieved with two US transducers and the AL: localized excitation with ROE of 190 µm (focused transducer with AL), localized excitation with ROE of 326 µm (focus transducer without AL), and wide-area excitation (unfocused transducer).

4.2. Sample preparation and characterization

In order to fabricate a side-by-side sample with a sharp mechanical step, the two sides of the sample were made up of a mixture of varying agar concentrations, which vary mechanical properties of resulting gel, and a fixed gelatin concentration. Maintaining a fixed gelatin concentration on both sides prevents blurring of the mechanical step due to osmosis across gelatin concentration gradient [49]. Effectively, the agar-in-gelatin mixture allows the two sides of the sample to be mechanically fused at the interface but still maintaining a sharp mechanical step [50]. Table 1 summarizes the concentrations and bulk mechanical properties (see Section 4.2.2 for mechanical testing procedure) of all individual agar-in-gelatin samples. The shear moduli of the four samples span a range of biologically relevant materials, from softer extracellular matrices to stiffer breast tumors [3,51–53].

Table 1. Agar concentrations and bulk mechanical properties of agar-in-gelatin samples. Remaining mass percentage consisted of 5% gelatin, 0.6% TiO_2, and distilled water. Shear moduli reflect mean ± standard deviation of 3 oscillatory shear rheometry measurements at 36 Hz.

Sample No.	Agar (% w/w)	Storage modulus, G' (kPa)	Loss modulus, G'' (kPa)
S1	0.75	0.43 ± 0.03	0.07 ± 0.01
S2	1.00	1.25 ± 0.05	0.20 ± 0.01
S3	1.25	1.65 ± 0.08	0.24 ± 0.01
S4	1.50	1.72 ± 0.06	0.25 ± 0.02

4.2.1. Preparation of agar-in-gelatin samples

To prepare the agar-in-gelatin mixture, gelatin powder (Sigma-Aldrich, G9391) was first added to half the final volume of distilled water in a centrifuge tube at room temperature and let bloom for approximately 5 minutes. The mixture was then kept at in a water bath at 75 °C for 60 minutes to let the gelatin dissolve. Meanwhile, solid agar (Fisher Scientific, BP1423) was added to the remaining volume of distilled water in a beaker and heated to approximately 90 °C with constant stirring on a magnetic hotplate stirrer until no solid pieces of agar could be observed. TiO_2

Biomedical Optics EXPRESS

particles with mean diameter of 500 nm were added to the beaker at a concentration of 0.6 % w/w to provide scattering. The mixture remained heated and stirred until the TiO_2 particles were roughly dispersed. Lastly, the agar mixture was added to the gelatin mixture in the centrifuge tube and mixed continuously with a vortexer for 60 seconds to achieve a homogeneous agar-in-gelatin mixture with uniformly dispersed TiO_2 particles.

Both homogeneous and side-by-side samples were prepared for imaging. Each sample was made in a 35-mm diameter petri dish with its bottom removed (to facilitate US transmission into the sample from below) and sealed with parafilm. First, 1% agar mixture was poured into the parafilm-bottomed petri dish in a vacuum desiccator to a thickness of approximately 2 mm, then, allowed to form a gel at room temperature to make a waterproof base (to prevent gelatin dissolution in water). For the homogenous samples, the prepared agar-in-gelatin mixtures were poured into separate petri dish over the agar base to a thickness of approximately 1 mm and desiccated until gelled at room temperature. For the side-by-side samples, a half-petri dish silicone blocker (Smooth-On, Ecoflex 00-10, molded in a petri dish then vertically cut in half) was placed flushed to one half of each petri dish before the S4 agar-in-gelatin mixture (Table 1) was poured into the remaining space to a thickness of approximately 1 mm; this made up the stiffer half of each side-by-side sample. After the S4 mixture gelled under desiccation at room temperature, the silicone blocker was carefully removed before the agar-in-gelatin mixture for the softer half was poured into the remaining space to match the thickness of the first half. Three configurations were prepared: S1-S4, S2-S4, and S3-S4, such that all side-by-side samples have the same absolute mechanical properties on the stiffer size (S4) but varying relative mechanical properties between the two sides.

We note that the samples were made necessarily thin (1 mm) to accommodate for the limited acoustic working distance afforded by our transducer and water bath setup when the AL was used. To address the potential contribution of reflected wave modes from the bottom boundary of the thin sample, we had verified in a separate experiment (with 326-μm ROE at 1.4-1.8 kHz) that responses obtained from 1-mm thick versus 4-mm thick samples were in good agreement (data not shown). In order to ensure consistent mechanical properties across different experimental conditions, all samples were made from the same batch of agar-in-gelatin mixtures, gelled in separate petri dishes under the same condition, and imaged after a fixed amount of time from pouring into the petri dishes. We have also verified in a separate experiment that multiple fabrications of the sample (i.e., separate petri dishes) from the same batch of mixture produced consistent experimental results (data not shown).

4.2.2. Bulk mechanical testing

Bulk mechanical properties of individual samples were obtained by parallel-plate shear rheometry (TA Instruments DHR-3) with oscillatory frequency-sweep test (0.1-100 Hz, 10-μN·m torque amplitude). Separate homogeneous samples were prepared from the same batches of agar-in-gelatin mixture for mechanical testing. The prepared agar-in-gelatin mixtures were poured into aluminum trays to a thickness of 2 mm, allowed to set, then, sealed with Saran wrap until testing. Immediately before testing each sample, the Saran wrap was removed, then, the sample was cut into a 40-mm diameter disk and placed on the rheometer plate. The top plate of the rheometer was lowered onto the sample until it registered an axial force of 0.1 N before the gap was fixed. The oscillatory test was repeated 5 times for each sample. Although the oscillatory frequency-sweep test was conducted up to 100 Hz, useful data could only typically be obtained below 40 Hz due to sample slippage and mechanical inertia of the rheometer fixture at higher frequencies.

4.3. Experimental designs

Two experiments were performed to experimentally quantify MIL and MSR metrics under different combinations of sample characteristics, excitation characteristics, and image acquisition

Biomedical Optics EXPRESS

schemes. Table 2 summarizes the experimental designs for the two experiments, which shall be referred to as Experiment 1 and Experiment 2 for the remainder of the paper.

Table 2. Experimental designs for the quantification of MIL and MSR metrics.

	Experiment 1: quantification of MIL	Experiment 2: quantification of MSR
Sample characteristics	Homogeneous samples S1, S2, S3, and S4.	Side-by-side samples S1-S4, S2-S4, and S3-S4.
Excitation characteristics	Localized excitation with ROEs of 326 μm and 190 μm, harmonically amplitude-modulated at frequencies in the range of 1-2 kHz.	Wide-area and localized excitations with ROEs of 326 μm and 190 μm, harmonically amplitude-modulated at frequencies in the range of 1.2-2-kHz.
Image acquisition	Off-axis detection with galvanometer-scanning of OCT beam and stationary ARF beam and sample.	On-axis detection with stage-scanning of sample and stationary (and coaxially aligned) ARF and OCT beams.
Response reconstructed	Amplitude of dynamic axial sample displacement, $U_z(x,z)$	Amplitude of dynamic uniaxial strain, $\varepsilon_{zz}(x,z)$
Metrics quantified	MIL metrics: HW_{HM} and HW_{1/e^2}	MSR metrics: Resolution, Contrast, and CNR

4.4. Data acquisition

First, the position of the US transducer was adjusted such that the ARF beam focused at the top surface of the sample and was coaxially aligned with the OCT beam at their initial positions at the center of the FOV. This process was repeated each time the sample or the US transducer was changed. Then, the peak-to-peak modulation amplitude (i.e., voltage sent to the function generator) was determined for each experimental condition (i.e., for each combination of sample, excitation ROE, and modulation frequency) in order to achieve optimal axial sample displacements. In Experiment 1, displacement amplitude in the range of 20-200 nm was maintained across the FOV to achieve detectable displacement at the edges of the FOV while remaining below the phase-wrapping limit at the point of excitation. In Experiment 2, displacement amplitude in the range of 40-60 nm was maintained on the stiffer side (S4) of the side-by-side samples across all experimental conditions. Average ratio of sample displacement amplitude to the displacement noise floor was in the range of 30-100 (relative signal power of 30-40 dB) in all datasets.

In Experiment 1, two 2D datasets with a transverse FOV of 3 mm were acquired by galvanometer-scanning of the OCT beam along the two orthogonal scanning axes (X and Y) for each combination of sample and excitation characteristics. Each dataset consisted of 4096 A-scans and 4 frames (at the same slow-axis position), corresponding to a transverse pixel size of 0.7 μm along the fast-axis. The line scan rate was varied with the modulation frequency to maintain a temporal sampling of 20 A-scans per modulation cycle.

In Experiment 2, two 3D datasets with a transverse FOV of 3 mm × 2 mm were acquired by stage-scanning of the side-by-side sample for each combination of sample and excitation characteristics: one from the softer side to the stiffer side, another from the stiffer side to the softer side. Both scan directions were implemented because they could potentially affect the elastogram obtained from harmonic localized ARF excitation (e.g., via mechanical wave propagation from one side to the other). Each dataset consisted of 16384 A-scans and 40 frames, corresponding to a transverse pixel size of 0.2 μm and 50 μm along the fast- and slow-axis, respectively. The line scan rate was kept at 20 kHz for all datasets. Although this resulted in lower temporal sampling per modulation cycles than in Experiment 1, the lowest temporal sampling (10 A-scans per modulation cycle at the highest 2-kHz modulation frequency) was still sufficient to detect the harmonic sample displacement response. The large number of A-scans per frame and the

Biomedical Optics EXPRESS

fixed line scan rate were implemented to keep the scanning velocity of the motorized stage low and constant across all datasets; this served to minimize the effect of water sloshing due to the motion of the sample (partially immersed in water) in each dataset.

4.5. Data processing

The following processing steps were performed on each frame of the raw data to obtain the oscillatory axial sample displacement response, $\tilde{u}_z(x,\ z,\ t) = U_z(x,\ z)\cos(\omega t - \varphi_{\text{drive}} - \varphi_u)$, with amplitude $U_z(x,z)$, angular frequency ω, and phase delay φ_u w.r.t. the excitation drive waveform. The arguments t, x and z denote the time, transverse (along fast axis) and axial coordinates at each pixel, respectively. We note that t and x are directly related by the line-scan rate in the on-axis detection scheme implemented in Experiment 2. All data processing steps were executed in MATLAB (R2017). First, space-domain OCT image was reconstructed from the raw data according to standard SD-OCT image reconstruction procedure (background subtraction, spectrum resampling, dispersion correction, and inverse Fourier transform). Then, $\tilde{u}_z(x,z,t)$ induced by the harmonic ARF excitation was computed using a previously reported phase-sensitive OCE reconstruction method [34]. Briefly, phase difference was calculated between adjacent A-scans to obtain axial sample velocity, median filtered with a 3×3 kernel, bandpass filtered (3$^{\text{rd}}$ order Butterworth filter, cutoffs at ± 40% of modulation frequency), then integrated along the fast axis to obtain axial sample displacement. This was filtered again by the same bandpass filter to obtain $\tilde{u}_z(x,z,t)$. Due to the large phase noise (i.e., large uncertainty in axial displacement measurement by phase-sensitive OCE) associated with low OCT SNR [54], pixels with OCT SNR less than 10 dB were considered unreliable and treated as missing values in subsequent processing steps to quantify MIL and MSR metrics.

4.5.1. Experiment 1: quantification of mechanical interaction length

Axial displacement amplitude $U_z(x,z)$ was obtained by first converting $\tilde{u}_z(x,z,t)$ to a complex-valued oscillatory response via a Hilbert transformation (along the fast axis) then computing its magnitude. Transverse profile of the axial displacement amplitude, $U_z(x)$, was obtained from the depth-average of $U_z(x,z)$ over 20 axial pixels (an axial range of 54 μm), starting from the pixel depth at approximately 50 μm below the top surface of the sample. The MIL metrics were quantified by first curve-fitting $U_z(x)$ to a sum of two Gaussian functions by nonlinear least-square curve-fitting, then, extracting HW_{HM} and HW_{1/e^2} from the best-fit curve. Given the displacement noise floor in the range of 0.6-1.5 nm, $U_z(x,z)$ values that were less than 8 nm (relative signal power < 15 dB, not to be confused with the 10-dB OCT SNR exclusion criteria) were considered unreliable because they were too close to the noise floor and treated as missing values (i.e., they did not contribute to the depth-averaging and curve-fitting operations). A sum of two Gaussian functions was used as the fitting function because it provided a good fit across all datasets; it does not hold any physical meaning pertaining to the physical response of the sample that can be presently identified. Nevertheless, it is noted that the axial sample displacement was not expected to retain the Gaussian transverse profile of the ARF excitation (insets of Fig. 3(b)) [55].

4.5.2. Experiment 2: quantification of mechanical step response

Dynamic uniaxial strain, $\tilde{\varepsilon}_{zz}(x,\ z,\ t) = \varepsilon_{zz}(x,\ z)\cos(\omega t - \varphi_{\text{drive}} - \varphi_\varepsilon)$, with amplitude $\varepsilon_{zz}(x,z)$, angular frequency ω, and phase delay φ_ε w.r.t. the excitation drive waveform, was estimated from least-square linear regression of $\tilde{u}_z(x,z,t)$ as a function of depth over 37 depth pixels (an axial window of 100 μm). We note that the phase delay φ_ε of the dynamic strain may not necessarily be equivalent to the phase delay φ_u of the dynamic sample displacement response. At each pixel

Biomedical Optics EXPRESS

depth i, the least-square linear regression is given by the equation:

$$\begin{bmatrix} \tilde{u}_z(x, z_i,\ t) \\ \tilde{u}_z(x, z_{i+1},\ t) \\ \vdots \\ \tilde{u}_z(x, z_{i+36},\ t) \end{bmatrix} = \begin{bmatrix} 1 & z_i \\ 1 & z_{i+1} \\ \vdots & \vdots \\ 1 & z_{i+36} \end{bmatrix} \begin{bmatrix} \beta_0 \\ \tilde{\varepsilon}_{zz}(x, z_i,\ t) \end{bmatrix}, \tag{4}$$

where z_i denotes the axial coordinate at the i^{th} pixel depth and β_0 is a linear regression constant. Uniaxial strain amplitude $\varepsilon_{zz}(x,z)$ was similarly obtained by converting to complex-valued oscillatory response and computing the magnitude. Transverse profile of the uniaxial strain amplitude, $\varepsilon_{zz}(x)$, was obtained from the depth-average of $\varepsilon_{zz}(x,z)$ over 9 depth pixels (an axial range of 24 μm), starting from the pixel depth at approximately 50 μm below the top surface of the sample in each A-scan (to account for uneven surface level along the transverse direction). The MSR metrics were quantified by first curve-fitting $\varepsilon_{zz}(x)$ to an error function (i.e., the integral of a Gaussian impulse response) by nonlinear least-square curve-fitting using the following fitting function:

$$\varepsilon_{zz,\ \text{fit}}(x) = \frac{a}{2}\left[1 \pm \text{erf}\left(\frac{x-b}{c}\right)\right] + d, \tag{5}$$

where a, b, c, and d are the curve-fitting variables. The ± sign in front of the error function accommodate for the two scan directions (– for scanning from softer to stiffer side, + for scanning from stiffer to softer side). Then, resolution, contrast, and CNR were calculated from the best-fit variables according to Eqs. (1)–(3), using $w = c$, $\mu_{\varepsilon,\ \text{soft}} = a + d$, and $\mu_{\varepsilon,\ \text{stiff}} = d$. For CNR, the standard deviation $\sigma_{\varepsilon,\ \text{soft}}$ and $\sigma_{\varepsilon,\ \text{stiff}}$ was calculated from $\varepsilon_{zz}(x)$ values starting from the edge of the FOV to approximately 550 μm away from the interface between the two sides.

4.6. Statistical analysis

Two types of statistical test were performed in MATLAB (R2017). First, multiple pairwise comparison based on Wilcoxon-type non-parametric Kruskal–Wallis test of variance was implemented to determine if there was a statistically significant difference in MIL and MSR metrics between a pair of ROEs or a pair of samples. Non-parametric test was implemented to accommodate for deviation from normal distribution (Anderson-Darling test for normality) and unequal variances (Bartlett test for equal variances) in the data. The sample sizes were $N = 88$ (11 frequencies, 2 scan axes, 4 frames per dataset) and $N = 720$ (9 frequencies, 2 scan directions, 40 frames per dataset) per test condition for the MIL and the MSR metrics, respectively. Reported p-value reflects the significance of χ^2 statistics on the group-adjusted (Bonferroni correction for multiple comparisons among groups) two-sided pairwise comparison; the difference was considered statistically significant if $p < 0.05$.

Second, Spearman rank correlation test was implemented to determine if there was a statistically significant correlation between a pair of an MIL metric and an MSR metric measured under different experimental conditions. The R^2 rank correlation coefficients are reported; the correlation was considered statistically significant if $p < 0.05$.

5. Results

5.1. Experiment 1: quantification of mechanical interaction length

In the off-axis acquisition scheme, localized ARF excitation of a homogeneous sample produced an axial displacement amplitude that peaked at the point of excitation (center of the FOV) on the sample surface and decayed as a function of distance away from the point of excitation

Biomedical Optics EXPRESS

(Fig. 4(a)). Comparisons of $U_z(x)$ normalized by its peak amplitude obtained with and without the AL from samples S1 (Fig. 4(b)) and S3 (Fig. 4(c)) showed that the displacement responses in both samples extended over a larger spatial range than the acoustic focal spot size of the ARF excitation for both 190-µm and 326-µm ROEs. Intuitively, a smaller ROE is expected to generate a more spatially-confined displacement response (i.e., smaller MIL) in the sample [20]. This was observed in sample S1, where the 190-µm ROE generated a narrower $U_z(x)$ profile than the 326-µm ROE at both $\mathrm{HW}_{\mathrm{HM}}$ and HW_{1/e^2} (Fig. 4(b)). However, in sample S3, the 190-µm ROE only generated a narrower $U_z(x)$ profile at $\mathrm{HW}_{\mathrm{HM}}$; the trend unexpectedly reversed at HW_{1/e^2}, where the 326-µm ROE generated a narrower response (Fig. 4(c)).

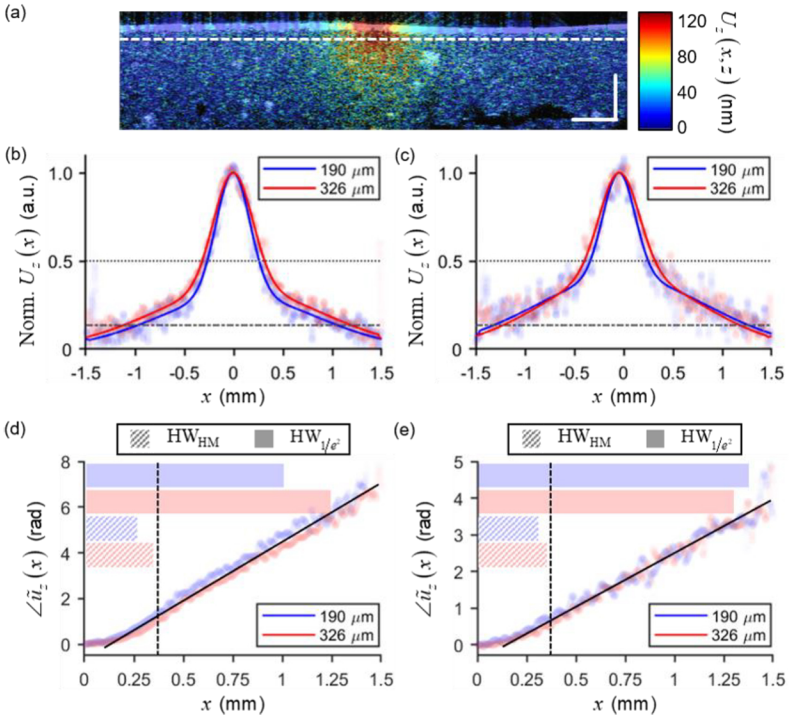

Fig. 4. Axial displacement responses to 1300-Hz localized ARF excitation in homogeneous samples. (a) Axial displacement amplitude map (color) overlaid on top of structural OCT image (grayscale) obtained from sample S1 with 190-µm ROE. Dotted line indicates approximate depth at which displacement was averaged to obtain $U_z(x)$. Scale bars: 250 µm. (b) and (c) $U_z(x)$ normalized by its maximum value as a function of x obtained with 190-µm (blue) and 326-µm (red) ROEs from samples S1 and S3, respectively. Data is shown in transparent markers. Solid lines correspond to the fit curves (coefficient of determination > 0.94, root mean squared error < 0.06). Black dotted and dashed lines indicate half and $1/e^2$ amplitude levels, respectively. (d) and (e) Phase angle of $\tilde{u}_z(x)$ as a function of x, overlaid with bar plots of $\mathrm{HW}_{\mathrm{HM}}$ (striped bar) and HW_{1/e^2} (solid bar) obtained with 190-µm (blue) and 326-µm (red) ROEs from samples S1 and S3, respectively. Data is shown in transparent markers. Black solid line highlights linear evolution of mechanical wave phase w.r.t. transverse propagation distance. Black vertical dashed line indicates the onset of this linear propagation region.

The transverse profiles of phase angle of the axial displacement response, $\angle\tilde{u}_z(x)$, showed that the observed displacement response could be described by two mechanisms (Figs. 4(d) and 4(e)). First, the sample within the vicinity of the ARF excitation "push region" was directly deformed

Biomedical Optics EXPRESS

by the applied acoustic pressure. This is evident by the relatively constant $\angle\tilde{u}_z(x)$ around the point of excitation ($x = 0$), followed by a non-linear evolution of $\angle\tilde{u}_z(x)$ as the direct deformation from the push extended to the adjacent region. Then, the displacement response transitioned into a mechanical wave "propagation region" (to the right of vertical dashed lines), where $\angle\tilde{u}_z(x)$ evolved linearly as a function of propagation distance. In both samples S1 and S3, HW_{HM} was reached before the onset of the induced mechanical wave propagation, whereas HW_{1/e^2} extended further into the propagation region. These observations supported the notion that HW_{HM} was predominantly a direct result of the applied stress distribution in the ROE, whereas HW_{1/e^2} depended on the characteristics of the induced mechanical wave propagating away from the point of excitation (refer to Section 3.1).

The trends in MIL observed in Fig. 4(b) and 4(c) were consistent across all modulation frequencies for both samples S1 and S3. Figure 5 shows that both HW_{HM} and HW_{1/e^2} were smaller with the 190-μm ROE than with the 326-μm ROE in sample S1 (Fig. 5(a) and 5(d)), whereas only HW_{HM} was smaller in sample S3 (Fig. 5(b) and 5(e)). In both samples, HW_{HM} and HW_{1/e^2} decreased with increasing modulation frequency. Boxplots of HW_{HM} from all modulation frequencies showed that the 190-μm ROE generated smaller HW_{HM} compared to the 326-μm ROE in all four samples, although the difference was not statistically significant in samples S2 and S4 (Fig. 5(c)). The same trend was observed for HW_{1/e^2} in samples S1 and S2, but was reversed in samples S3 and S4, where the 326-μm ROE generated smaller HW_{1/e^2} than the 190-μm ROE (Fig. 5(f)).

To further investigate this unexpected sample-dependent reversal in the trend between ROE and ROR, we analyzed the correlation between the effect of ROE on ROR and the bulk mechanical properties of the sample (Fig. 6). The effect of ROE on ROR is quantified by relative MIL, defined as the ratio of MIL metrics obtained with the 190-μm ROE to those obtained with the 326-μm ROE (i.e., relative MIL < 1 indicates a decrease in ROR with smaller ROE). The relative HW_{1/e^2} showed a stronger correlation ($R^2 = 0.81$) to both stiffness (given by the magnitude of complex shear modulus, $|G^*|$) and relative viscosity (given by the loss ratio, G''/G') of the samples, whereas the relative HW_{HM} only showed a weak correlation ($R^2 = 0.24$). These observations further reinforced the distinction between the two mechanisms governing HW_{HM} and HW_{1/e^2}. Mechanical properties of the sample had relatively little influence on the effect of ROE on HW_{HM}, which is predominantly a direct result of the ARF "push". On the other hand, sample mechanical properties had a profound influence on the effect of ROE on HW_{1/e^2}, which reflects the characteristics of mechanical wave propagation (e.g., wave speed and attenuation). We note that no quantitative comparison between the absolute bulk mechanical properties from shear rheometry (obtained at 36 Hz) and our ARF-OCE results (obtained at 1-2 kHz) was made due to the frequency-dependent viscoelasticity of the samples. We used the relative mechanical properties between samples to complement the interpretation of our results.

5.2. Experiment 2: quantification of mechanical step response

In the on-axis acquisition scheme, localized ARF excitation of a stage-scanned side-by-side sample produced a uniaxial strain map that exhibited a gradual transition from higher to lower strain at the interface between the softer (left) and the stiffer (right) sides (Fig. 7(a)). Comparisons of $\varepsilon_{zz}(x)$ normalized by the relative acoustic power of the ARF excitation, P_{ARF}, obtained with different excitation ROEs showed that, for a given total acoustic power, larger strain was generated on both sides of the sample when the acoustic power was localized to a more confined space (Fig. 7(b)). P_{ARF} is defined as the product of relative acoustic transmission (0.67 with AL and 1 without AL) and the square of modulation amplitude voltage (refer to Section 4.4). We note that this normalization was only to observe the effect of ARF localization on the resulting strain amplitude; the MSR metrics were computed directly from the measured $\varepsilon_{zz}(x)$ without

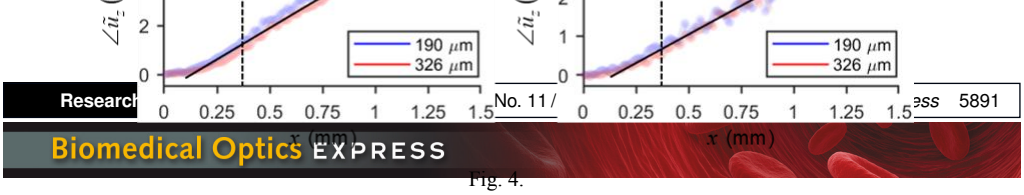

Fig. 4.

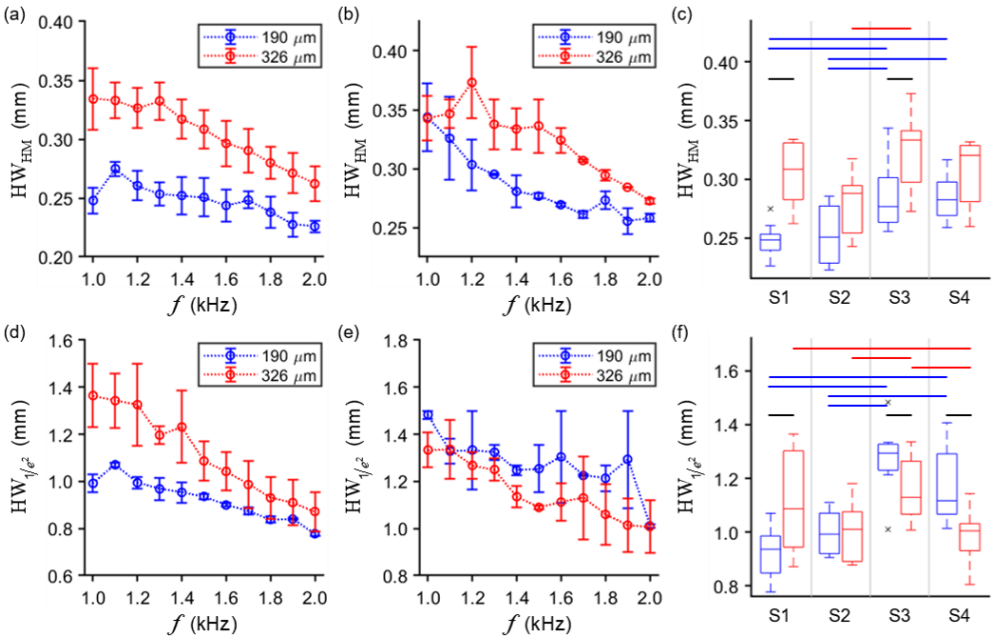

Fig. 5.

Fig. 5. Effect of ROE on ROR based on experimentally quantified MIL metrics. HW_{HM} and HW_{1/e^2} as a function of modulation frequency, f, obtained with 190-μm (blue) and 326-μm (red) ROEs in (a) and (d) sample S1, and (b) and (e) sample S3. Error bars represent ± 1 standard deviation from 8 measurements (2 scan directions, 4 frames each). There was no statistically significant difference between the X and Y scan directions (data not shown). (c) and (f) Boxplots of HW_{HM} and HW_{1/e^2} from all f obtained with 190-μm (blue) and 326-μm (red) ROEs in each sample (separated by vertical lines). Whiskers represent approximately ± 3 standard deviation (if the data were normally distributed); data outside of this range are considered outliers and shown in black markers. Horizontal bars indicate statistically significant pairwise difference between two conditions: black bars for comparisons between two ROEs in each sample, blue bars for comparisons between two samples with the 190-μm ROE, and red bars for the comparisons between two samples with the 326-μm ROEs.

normalization, as described in Section 4.5.2. Comparisons of $\varepsilon_{zz}(x)$ normalized between 0 (stiffer side) and 1 (softer side) showed the effect of ROE on the sharpness of the mechanical step as it appeared on the uniaxial strain elastogram (Fig. 7(c)). A sharper step was obtained with the 190-μm ROE compared to the 326-μm ROE, consistent with the conjecture that a smaller ROE would produce an elastogram with higher spatial resolution [17–20]. However, the sharpest step was obtained with the wide-area excitation; a completely opposite trend from the observation in the localized excitation cases based on the definition of ROE adopted in this paper.

The comparisons between ROEs observed in Fig. 7(b) and 7(c) were consistent across all modulation frequencies in sample S1-S4 (Fig. 8(a)–8(c)). Unlike the MIL metrics (Fig. 5), no conclusive trend as a function of modulation frequency could be identified over the investigated frequency range for the MSR metrics. However, further investigation over larger frequency range may lead to more apparent trends. For spatial resolution, a general decreasing trend with increasing modulation frequency could be observed for the wide-area excitation and the localized excitation with 326-μm ROE, but this trend was less prominent for the 190-μm ROE (Fig. 8(a)).

Biomedical Optics EXPRESS

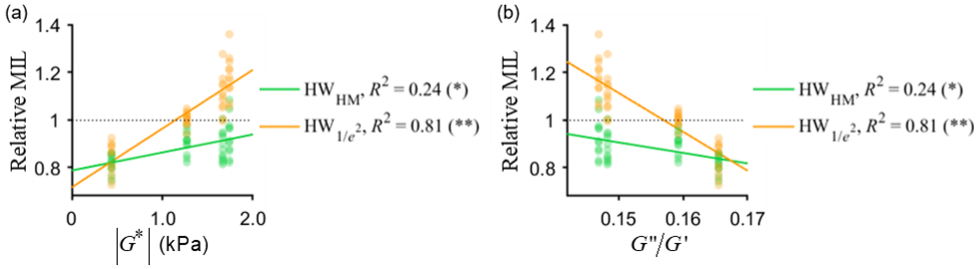

Fig. 6.

Fig. 6. Correlation between sample mechanical properties and the effect of ROE on ROR. (a) and (b) Linear regressions of relative HW_{HM} (green) and relative HW_{1/e^2} (orange) from all f (1-2 kHz) as a function of magnitude of complex shear modulus, $|G^*|$, and loss ratio, measured by shear wave elastography. Indicated statistical significance of correlation ($^*p < 0.05$, $^{**}p < 0.01$). Relative MIL < 1) and vice versa.

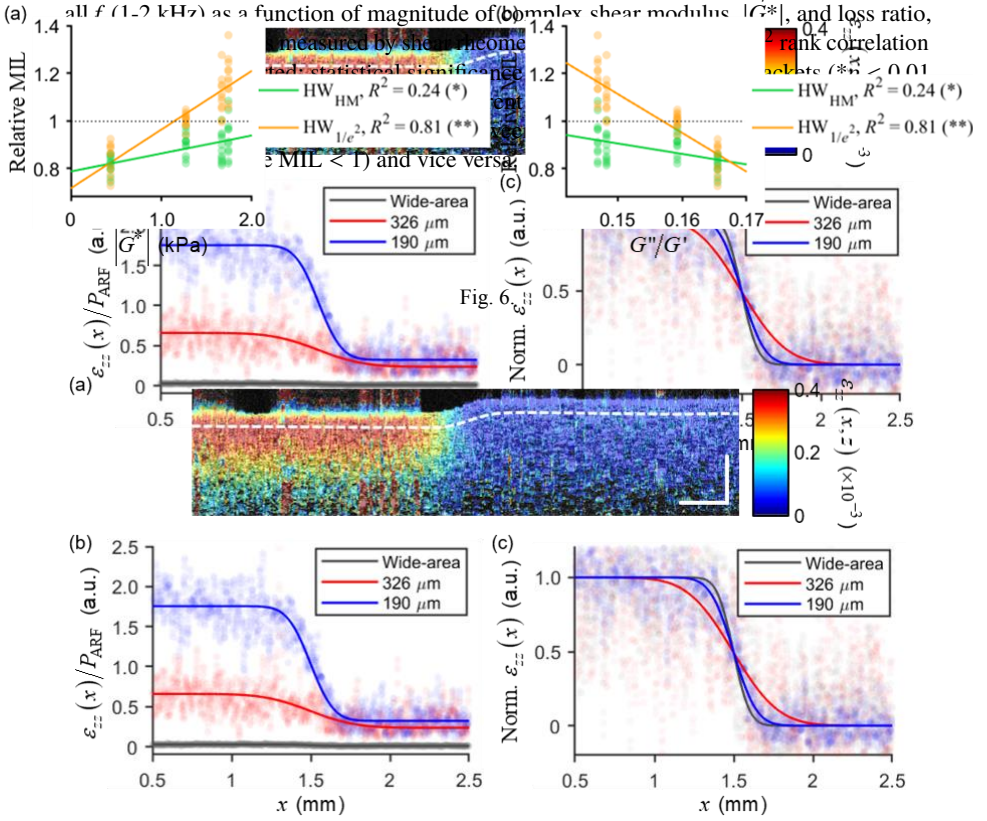

Fig. 7.

Fig. 7. Uniaxial strain elastogram obtained from 1400-Hz ARF excitation in side-by-side samples. (a) Uniaxial strain map (color) overlaid on top of structural OCT image (grayscale) obtained from side-by-side sample S1-S4 (S1 on the left, S4 on the right) with 190-μm ROE. Dotted line indicates approximate depth at which strain was averaged to obtain $\varepsilon_{zz}(x)$. Scale bars: 250 μm. (b) $\varepsilon_{zz}(x)$ normalized by relative ARF power, P_{ARF}, as a function of x obtained with 190-μm ROE (blue), 326-μm ROE (red), and wide-area excitation (gray) in sample S1-S4. (c) Results in (b) normalized between 0 and 1 for comparison of the sharpness of mechanical step on the uniaxial strain elastogram. In (b, c), data is shown in transparent markers. Solid lines correspond to the fit curves (coefficient of determination 0.65, 0.64, and 0.91 for wide-area excitation, 326-μm ROE, and 190-μm ROE, respectively).

Biomedical Optics EXPRESS

For contrast, the localized excitation with both 190-μm and 326-μm ROEs demonstrated an increasing trend with increasing modulation frequency, but the wide-area excitation showed a decreasing trend (Fig. 8(b)). Similarly, for CNR, both localized excitation cases showed a monotonically increasing trend with increasing modulation frequency whereas the wide-area excitation showed the opposite (Fig. 8(c)).

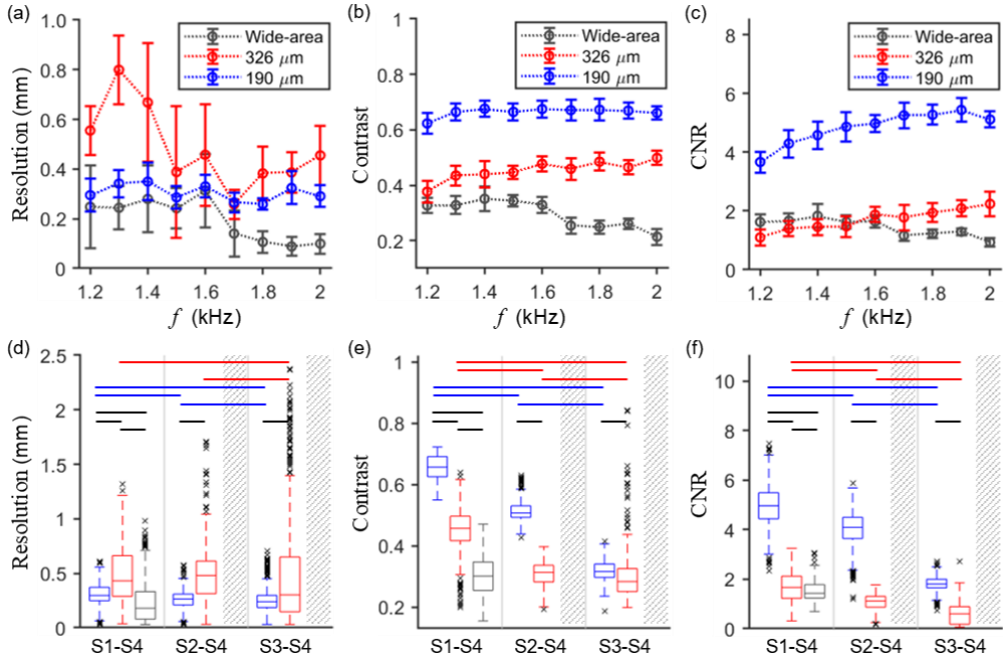

Fig. 8.

Fig. 8. Effect of ROE on elastogram quality based on experimentally quantified MSR metrics. (a)–(c) Resolution, contrast, and CNR as a function of modulation frequency, f, obtained with 190-μm ROE (blue), 326-μm ROE (red), and wide-area excitation (gray) in side-by-side sample S1-S4. Error bars represent ± 1 standard deviation from 80 measurements (2 scan directions, 40 frames each). There was no statistically significant difference between the two scan directions (data not shown). (d)–(f) Boxplots of resolution, contrast, and CNR from all f obtained with 190-μm ROE (blue), 326-μm ROE (red), and wide-area excitation in each side-by-side sample (separated by vertical lines). Whiskers represent approximately ± 3 standard deviation (if the data were normally distributed); data outside of this range are considered outliers and shown in black markers. Horizontal bars indicate statistically significant pairwise difference between two conditions: black bars for comparisons between two ROEs in each sample, blue bars for comparisons between two samples with the 190-μm ROE, and red bars for the comparisons between two samples with the 326-μm ROEs. Data for wide-area excitation is only available for side-by-side sample S1-S4.

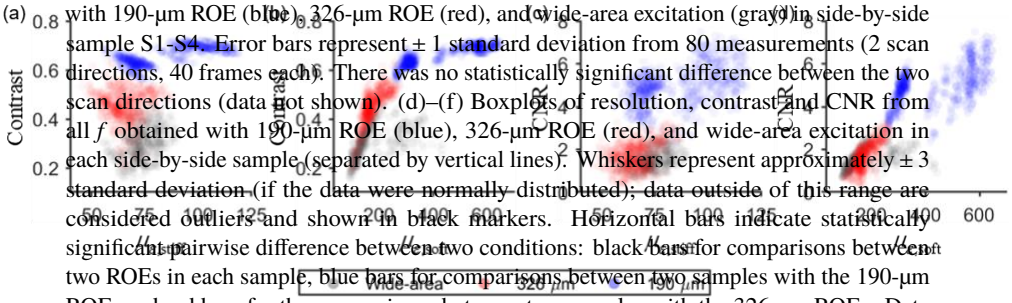

Fig. 9.

Boxplots of spatial resolution, contrast, and CNR from all modulation frequencies showed that the 190-μm ROE resulted in superior strain elastogram quality based on all three MSR metrics compared to the 326-μm ROE in all three side-by-side samples (Fig. 8(d)–8(f)). This outcome is not only in agreement with the conjecture that spatial localization of the excitation would improve spatial resolution of the elastogram, but also suggests that the effect of smaller ROE applies to enhancing contrast and CNR as well. Interestingly, the same trend as a function of ROE extended to the wide-area excitation for contrast and CNR, but not spatial resolution. The resolution metric of the wide-area excitation was significantly smaller (i.e., higher resolution) than both localized excitation cases for side-by-side sample S1-S4 (Fig. 8(d)). We note that the wide-area excitation

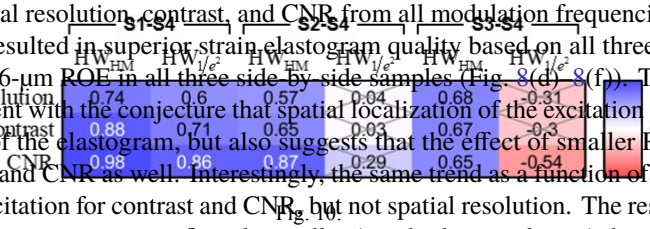

Fig. 10.

Biomedical Optics EXPRESS

was unable to generate sufficiently large displacements in the stiffer samples due to the acoustic power being distributed over a large area (Fig. 8(b)), thus, wide-area results are only available for side-by-side sample S1-S4. This outcome is in contradiction of the conjecture that a smaller ROE would produce an elastogram with higher spatial resolution, based on the definition of ROE adopted in this paper.

The differences in resolution, contrast, and CNR were also observed between different side-by-side samples. Contrast and CNR expectedly decreased as the actual stiffness contrast (i.e., ratio of shear moduli) between the two sides reduced from side-by-side sample S1-S4 to side-by-side sample S3-S4 (Fig. 8(e) and 8(f)). Notably, spatial resolution improved as the stiffness contrast decreased for both the 190-μm and the 326-μm ROEs; the trend being statistically significant across all three side-by-side samples for the 190-μm ROE (blue bars in Fig. 8(d)). This trend was opposite to that observed by Hepburn et al. with bulk compression OCE, where lateral feature resolution of a stiff inclusion in a softer bulk was found to improve as the inclusion was made stiffer [30]. This finding was attributed to the narrowing of the gradient in uniaxial strain within the inclusion as it became stiffer and experienced smaller deformation [30]. In our experiments, when the localized ARF excitation was applied near the interface, the displacement response was induced on both sides of the sample, with the softer side experiencing larger deformation. Through the coupled interface between the two sides, the displacement response on the softer side was restricted by the presence of the less deformed stiffer side, giving rise to the gradient in uniaxial strain on the softer side that degraded the spatial resolution. This restrictive effect decreases as the mechanical properties of the softer side approaches that of the stiffer side (whose mechanical properties were kept the same in all three side-by-side samples), resulting in better resolution in samples with lower stiffness contrast.

The improvement in contrast and CNR with smaller ROE can also be examined in the context of the restrictive effect described above. First, we verified that the higher contrast and CNR observed with smaller ROE were not simply due to larger acoustic force per unit area causing an overall larger deformation in the sample [56]. Scatter plots of contrast and CNR measured in side-by-side sample S1-S4 against median uniaxial strain amplitude on the stiffer side (S4) showed that the improvement in contrast and CNR was apparent even when $\mu_{\varepsilon,\,\mathrm{stiff}}$ was kept consistent across all three excitation configurations (see Section 4.4) (Figs. 9(a) and 9(c)). Although a range of larger $\mu_{\varepsilon,\,\mathrm{stiff}}$ was induced in some spatial locations (out of the 40 slow-axis positions) for the 190-μm ROE, this variation in strain was not correlated to variation in contrast and CNR. (We note that if higher ARF excitation power were to be used such that larger uniaxial strain amplitude was induced on both sides of the sample, we would observe higher contrast and CNR in all cases (data not shown) due to the effect of strain amplitude on the ratio $\mu_\varepsilon/\sigma_\varepsilon$ [56].) On the other hand, the increase in uniaxial strain amplitude on the softer side (S1) showed a strong correlation with both contrast and CNR (Figs. 9(b) and 9(d)). These results imply that when similar uniaxial strain amplitude was induced on the stiffer side, the excitation with a smaller ROE was able to induce larger deformation on the softer side. In other words, localization of the ARF excitation to a smaller ROE diminished the restrictive effect imposed by the presence of the stiffer side on the displacement response of the softer side. Given that the ratio $\mu_\varepsilon/\sigma_\varepsilon$ is expected to increase with larger strain amplitude [56], excitation with a smaller ROE is expected to enhance both contrast and CNR of the elastogram.

5.3. Correlation between mechanical interaction length and mechanical step response

In order to investigate the hypothesis that a smaller ROE enhances the spatial resolution of the final elastogram via spatial confinement of the sample displacement response (i.e., smaller ROR), we analyze the correlation between MIL (characterizing the ROR) and MSR (characterizing the elastogram quality) metrics. Spearman R rank correlation coefficients between the MSR metrics quantified in each side-by-side sample and the MIL metrics quantified in the corresponding

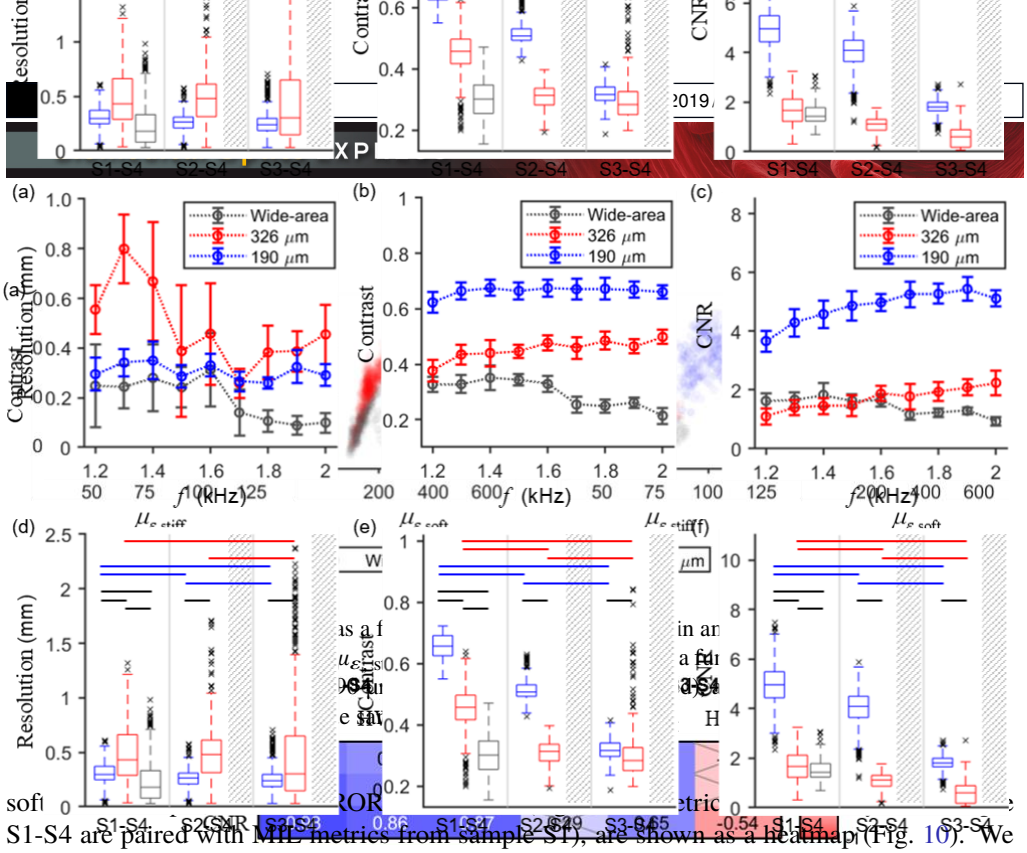

Fig. 9.

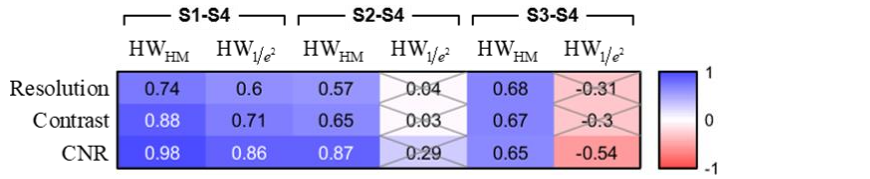

Fig. 10.

Fig. 10. Heatmap of Spearman R rank correlation coefficient between MIL metrics and MSR metrics. MSR metrics quantified in a side-by-side sample is analyzed w.r.t. MIL metrics quantified in the corresponding softer-side sample (e.g., MSR metrics from side-by-side sample S1-S4 are paired with MIL metrics from sample S1). $N = 18$ measurements per sample (2 ROEs, 9 modulation frequencies each). $R > 0$ (blue) indicates smaller ROR correlates to superior elastogram quality. $R < 0$ (red) indicates smaller ROR correlates to worse elastogram quality. Cross indicates that the correlation is not statistically significant at 95% confidence interval.

Scatter plots of MSR metrics as a function of MIL metrics for selected representative correlation pairs are shown in Fig. 11. We note that although linear fit lines are shown to aid visualization in

Biomedical Optics EXPRESS

Fig. 11, the statistical analysis of correlation between MIL and MSR metrics does not depend on the linearity of the relationships. A smaller ROR, as quantified by both HW_{HM} (Fig. 11(a)–11(c)) and HW_{1/e^2} (Fig. 11(e)–11(g)), demonstrated a statistically significant correlation to an improved elastogram quality, as quantified by all three MSR metrics, in side-by-side sample S1-S4. Meanwhile, a smaller HW_{HM} was correlated to an improved elastogram quality based on all three MSR metrics in side-by-side sample S2-S4, but the correlation was not statistically significant for HW_{1/e^2} (Fig. 10, scatter plots not shown). Lastly, a smaller HW_{HM} was likewise correlated to an improved elastogram quality in side-by-side sample S3-S4, but a smaller HW_{1/e^2} conversely correlated to a degraded elastogram quality (red shading in Fig. 10); representative scatter plots are shown for resolution versus HW_{HM} (Fig. 11(d)) and CNR versus HW_{1/e^2} (Fig. 11(h)).

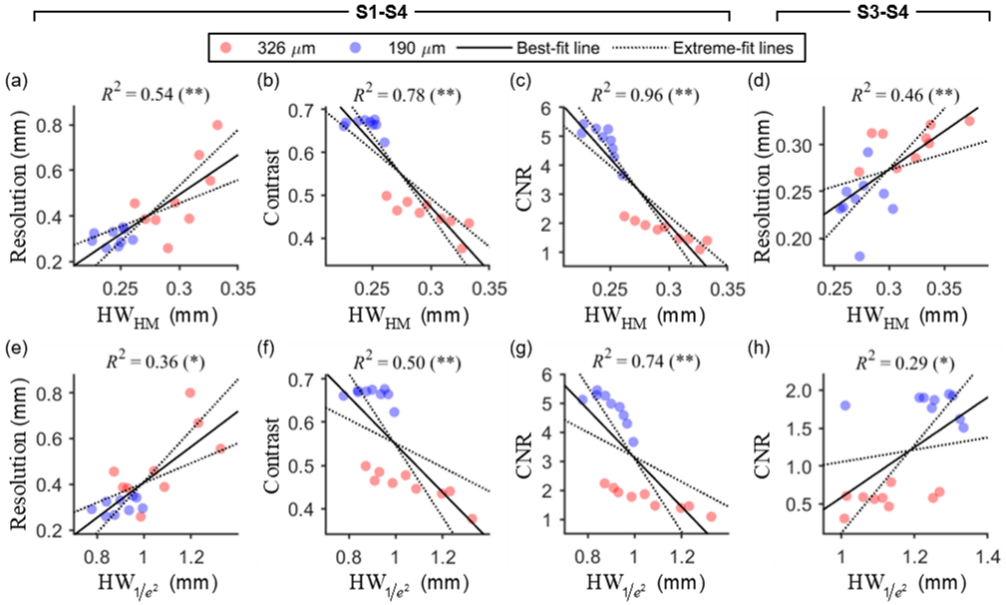

Fig. 11. Correlation between ROR characterized by MIL metrics and elastogram quality characterized by MSR metrics. (a)–(c) and (e)–(g) Resolution, contrast, and CNR quantified in side-by-side sample S1-S4 as a function of HW_{HM} and HW_{1/e^2} quantified in sample S1. (d) and (h) Resolution and CNR quantified in side-by-side sample S3-S4 as a function of HW_{HM} and HW_{1/e^2} quantified in sample S3. Spearman R^2 rank correlation coefficients are reported; two-tailed statistical significance is indicated the in the brackets ($*p < 0.05$ and $**p < 0.005$). 18 data points (2 ROEs, 9 modulation frequencies each) are shown in transparent markers. Solid and dotted lines represent the linear best-fit and extreme-fit lines, respectively.

6. Discussion

6.1. Reconstruction of elastogram based on dynamic uniaxial strain

The harmonic ARF excitation induced a dynamic oscillatory displacement response at the modulation frequency in our dynamic ARF-OCE measurements. This dynamic displacement response added a layer of complexity to the reconstruction of uniaxial strain that is typically computed in quasi-static compression OCE [30–32]. In Experiment 2, uniaxial strain was computed from the derivative of the oscillatory axial displacement response w.r.t. the axial

Biomedical Optics EXPRESS

distance (see Section 4.5.2). The outcome of this reconstruction was a dynamic oscillatory uniaxial strain response; the amplitude of which was computed to obtain the final uniaxial strain elastogram (Fig. 7(a)). The strain elastogram reconstruction implemented here is unlike the traditional static uniaxial strain calculation employed in quasi-static compression OCE, where a spatial derivative is simply computed from the sample displacement between the loaded and unloaded states [30–32].

The reconstruction of a strain map is not unprecedented in dynamic OCE. However, to our knowledge, this is the first time that a dynamic strain elastogram has been computed from the dynamic (time-varying) displacement response. Existing dynamic OCE approaches have typically been based on the sample displacement response, which can then be used to compute properties such as the shear wave speed in the off-axis detection scheme [25–27,35–37], or the elastogram can be obtained directly from the displacement amplitude in the on-axis detection scheme [34,39]. Our uniaxial strain elastogram, obtained from the amplitude of oscillatory uniaxial strain response, is analogous to the axial displacement amplitude map produced in existing dynamic OCE approaches [29,34,39]. However, strain amplitude as a parameter may provide a more intuitive inference to the mechanical properties of the sample compared to displacement amplitude. Uniaxial strain maps have been previously reconstructed from the displacement amplitude map by computing the derivative of the displacement amplitude (i.e. magnitude) w.r.t. the axial depth [57,58]. This approach inherently assumed that the sample displacement response was exactly in-phase along the axial direction because any information on the phase delay of the displacement response w.r.t. the applied stress has been lost by taking its amplitude prior to computing the axial derivative. In this paper, we computed the axial derivative of the dynamic displacement response (i.e. with its amplitude and phase information intact) directly to obtain a dynamic oscillatory uniaxial strain response (with its own amplitude and phase). Although not investigated in this study, map of the phase delay w.r.t. excitation drive waveform of the dynamic strain, φ_{ε}, may provide an additional contrast to highlight mechanical heterogeneity within the sample, in analogous fashion to the displacement phase map [29,34,39].

It is worth comparing the spatial resolution of our dynamic strain elastogram to that of typical static strain elastogram in compression OCE. Our wide-area excitation produced dynamic strain elastograms with median (across 9 modulation frequencies) spatial resolution of 180 µm, which is within the range of values measured by Hepburn et al. for lateral feature resolution in quasi-static compression OCE [30]. Furthermore, the median spatial resolutions achieved by our localized excitation schemes (290 µm for 190-µm ROE, 430 µm for 326-µm ROE), although by comparison are worse than the resolution obtained with wide-area excitation, are not inferior to the lateral feature resolution reported by Hepburn et al. for large inclusion size (which more closely resembles our side-by-side sample configuration) [30].

6.2. Impact of region of excitation on region of response and elastogram quality

We experimentally investigated the effect of spatial localization of the ARF excitation on the transverse spatial extent of the sample displacement response and the image quality of the resulting uniaxial strain elastogram. In Experiment 1, we found that a more spatially confined ARF excitation (ROE of 190 µm versus 326 µm) produced a displacement response that spanned a smaller transverse spatial extent in all four samples based on the HW_{HM} MIL metric (Fig. 5(a)–5(c)). This trend supports the conjecture that a smaller ROE would result in a smaller ROR. However, an unexpected sample-dependent reversal in the relationship between ROE and ROR was found based on the HW_{1/e^2} MIL metric (Fig. 5(d)–5(f)). To our knowledge, the sample-dependent reversal in the trend between ROE and ROR experimentally observed here has not been recapitulated in existing analytical models of sample displacement response to localized mechanical excitation [55,59]. The response of the sample to localized ARF excitation may be considered as a combination of two effects: deformation caused directly by the applied

Biomedical Optics EXPRESS

stress distribution in the ROE (characterized by HW_{HM}) and sample displacement corresponding to the propagation of mechanical wave away from the ROE (characterized by HW_{1/e^2}) (Figs. 4(d) and 4(e)). Indeed, we found that compared to HW_{HM}, the effect of ROE on HW_{1/e^2} is more strongly correlated to both stiffness and relative viscosity of the sample (Fig. 6) since propagation of mechanical wave is highly dependent on mechanical properties. These results suggest that the effect of ROE on the ROR is increasingly dependent on the mechanical properties of the sample as the relative contribution of the latter effect on the physical response of the sample becomes more dominant.

In Experiment 2, we found that localized ARF excitation with a smaller ROE produced a uniaxial strain elastogram with superior spatial resolution, contrast and CNR compared to a larger ROE in all three side-by-side samples (Fig. 8). These results support and extend the conjecture that spatial localization of the excitation would improve not only the spatial resolution but also contrast and CNR of the elastogram. However, the extreme case of wide-area excitation appears to deviate from this trend for spatial resolution, where it produced the highest resolution elastogram out of all three excitation schemes in side-by-side sample S1-S4 (Fig. 8(d)). Under the premise that the ROR connects between the ROE and the elastogram quality, this apparent discrepancy may arise from the fact that the ROR cannot be quantitatively characterized for wide-area excitation based on the MIL metrics defined in this paper. Whereas the physical response is a combination of both the direct deformation by the applied stress and the sample displacement due to the induced mechanical wave under localized excitation, it is predominantly caused by the former effect under wide-area excitation (the entire FOV being within the "push region"). Different relative contributions from each component of the strain tensor underlie these two effects—where uniaxial strain dominates in the direct deformation by the applied axial stress, shear strain (which involves both transverse and axial components) plays a larger role in the propagation of an induced mechanical wave from a localized source of vibration. This difference in the mechanisms underlying the physical response of the sample may have to be considered in order to reconcile the experimental results obtained with localized versus wide-area excitations.

6.3. Correlation between region of response and elastogram quality

It has been proposed that the spatial localization of mechanical excitation influenced the spatial resolution of the elastogram by confining the physical response of the sample to a limited spatial range [19,20]. Indeed, the high degree of spatial localization of mechanical excitation, and the detection of the resulting response at the point of excitation, is thought to play a key role in the high spatial resolution provided by AFM for quantifying spatially varying mechanical properties [21–24]. From the correlation between MSR and MIL metrics, we found that a more spatially confined ROR was correlated to an improved elastogram quality based on all three MSR metrics in side-by-side sample S1-S4 (Fig. 10). This result is in support of the hypothesis that the ROR, which is affected by the ROE, does impact the quality of the elastogram. Notably, a stronger correlation was found between the MSR metrics and HW_{HM} compared to HW_{1/e^2} (Fig. 10), which may imply that the uniaxial strain elastogram obtained in Experiment 2 was influenced to a greater extent by the direct deformation of the sample due to the applied stress in the ROE compared to the sample displacement due to mechanical wave propagation. Further supporting this implication is the finding that smaller HW_{1/e^2} correlates to worse elastogram quality based on all three MSR metrics in side-by-side sample S3-S4 (Fig. 10), which was a consequence of the sample-dependent reversal in the trend between ROE and HW_{1/e^2} in Experiment 1 (Figs. 5(d)–5(f)). These results may reflect the nature of the on-axis detection scheme adopted in Experiment 2; since the measured sample displacement response was obtained at the point of excitation, it was affected to a greater extent by the physical response of the sample around the point of excitation compared to further away.

Biomedical Optics EXPRESS

Our current results and analysis are not sufficient to conclusively prove or disprove the hypothesis that a smaller ROE improves the spatial resolution of the elastogram via spatial confinement of the physical response to a smaller ROR. However, our results do suggest that the ROR may indeed connect between the ROE and the quality of the elastogram. We also note that the characterization of ROR by a quantitative metric, in a manner that is a meaningful measure of the elastogram quality, is not trivial and may have to be defined on a system-specific basis. For the system adopted in Experiment 2, where response was measured at the point of excitation by the on-axis detection scheme, HW_{HM}, which predominantly reflects the direct deformation of the sample by the applied stress in the ROE, is a better predictor for elastogram quality than HW_{1/e^2}. On the other hand, for other quantitative OCE approaches based on measurements of mechanical wave propagation with an off-axis detection scheme [25–27,35,37,40], HW_{1/e^2} or other alternative MIL metrics that better capture the characteristics of the induced mechanical wave may be more predictive of the elastogram quality. Thus, our definition of the ROR may need to be reconsidered for each specific elastography system (such as systems employing wide-area excitation) and application in order to draw a mechanistic connection between the physical response of the sample and the quality of the obtained elastogram.

6.4. *Possible extension of current experiments and implications for elastography applications*

Several extension and improvements can be made to the experiments presented in this paper to further understand the various factors that contribute to the elastogram quality in dynamic ARF-OCE. First, this type of experimental characterization studies in elastography may benefit from the development of a standardized resolution target, akin to the USAF target in optical microscopy. In this paper, we fabricated the side-by-side samples containing a sharp mechanical step by using hand-cut silicone blocker (see Section 4.2.1), which inherently could not produce an ideal Heaviside step function-like interface at the micrometer length scale of the OCE measurements [10–12]. The use of such custom-made tissue-mimicking samples prevents quantitative comparisons of elastogram quality metrics across different studies—a remaining challenge in the field of OCE. A standardized OCE resolution target, obtained with controlled micro-fabrication processes such as stereolithography [60] and photopolymerization [61] technologies, may address this limitation in the field.

Second, quantitative investigation of the relationship between ROE, ROR, and elastogram quality may benefit from capturing the full tensorial strain field, including both uniaxial and shear components, in the sample response. Our presented experimental method based on phase-sensitive OCE reconstruction [34] is only able to measure the axial sample displacement. As a result, only the uniaxial strain could be reconstructed from our measurements; the shear strain, given by $\tilde{\gamma}_{xz} = \partial\tilde{u}_z/\partial x + \partial\tilde{u}_x/\partial z$, could not be calculated without the measurements of transverse sample displacement. An alternative approach is to combine the current axial displacement measurement method with other OCE methods for transverse displacement measurement [62–65] to reconstruct the full strain tensor. Access to the full tensorial strain field may help reconcile the conflicting trends observed between localized versus wide-area excitation schemes in our experiments (see Section 6.1).

Our experimental results on the effect of spatial localization of the ARF excitation on the elastogram quality suggest that localized excitation with a smaller ROE is preferable to one with a larger ROE for dynamic ARF-OCE of soft viscoelastic samples. For localized excitation, a more spatially confined mechanical excitation not only improves the spatial resolution of the strain elastogram, but also enhances its contrast and CNR. Conversely, when compared to wide-area excitation, the spatial resolution for both localized excitation schemes in our experiments was inferior, suggesting that a wide-area excitation may be the most suitable for maximizing the spatial resolution of the elastogram. However, whether wide-area excitation offers the highest

Biomedical Optics EXPRESS

spatial resolution, or if localized excitation with a sufficiently small ROE (i.e., smaller than the 190-μm ROE in this paper) would be able to exceed that limit, cannot be concluded from currently available results and must be further investigated. Nevertheless, our results suggest that minimizing the ROE is desirable for distinguishing small differences in mechanical properties, or when deformation is expected to be small, owing to the superior contrast and CNR that localized excitation with a smaller ROE offers.

Furthermore, our analysis of correlation between ROR and elastogram quality suggests that the ROR may provide an additional metric that informs the design of an elastography system. For instance, it may prove beneficial to approach the design of an elastography system that utilizes localized mechanical excitation from the perspective of minimizing the resulting ROR (as opposed to just minimizing the ROE) in order to optimize spatial resolution, contrast, and CNR of the elastogram. In this case, the ROR is a more comprehensive representation of the elastography system than the ROE alone, because it reflects the contributions of not only the excitation characteristics, but also other factors that ultimately influence the measured response of the elastography system (Fig. 1). However, more rigorous studies, both theoretically and experimentally, are still needed before a quantitative connection between the ROR and the quality of the elastogram can be made. Importantly, this relationship as well as the definition of the ROR itself will likely have to be investigated on a case by case basis for specific elastography systems and applications.

In addition, a more rigorous investigation on the relationships between ROE, ROR, and elastogram quality should also explore a wider range of sample mechanical properties (absolute and relative) and mechanical excitation characteristics (spatial and temporal). The effects of sample viscosity and excitation frequency may be particularly important. Viscosity is expected to have a profound effect on the ROR due to the attenuation of the displacement response associated with viscous loss [37]. Similarly, ROR was found to decrease with increasing modulation frequency (Fig. 5) due to the frequency-dependent attenuation of the viscoelastic samples. Given the correlation between the ROR and elastogram quality, both viscosity and excitation frequency are expected to influence resolution, contrast and CNR of the elastograms. Although resolution was found to improve from side-by-side sample S1-S4 to side-by-side sample S3-S4, this finding was attributed to the relative stiffness contrast between the samples and the restrictive effect of being mechanically coupled to a stiffer side. In order to independently investigate the effect of viscosity, the viscosity of the sample should be varied while maintaining constant stiffness contrast, such as with the addition of oil to agar-in-gelatin phantom [66]. Meanwhile, the improvement in contrast and CNR as a function of increasing modulation frequency is already apparent from our results with localized ARF excitations (Figs. 8(b) and 8(c)). However, a larger frequency range should be investigated in order to validate the role of excitation frequency on resolution, contrast, and CNR. The outcome of this study could have an important implication on the experimental design of dynamic OCE, where it may be desirable to operate at a higher modulation frequency in order to confine the ROR to a smaller spatial range and enhance the quality of the elastograms as a result.

Lastly, we emphasize that the results presented in this paper are specific to uniaxial strain elastograms obtained with dynamic ARF-OCE using continuous harmonic excitation in soft tissue-mimicking samples. Although it may be possible that similar results would be observed in other OCE systems, the results and their implications as derived from our presented experiments cannot be readily generalized to any OCE systems. For instance, the MIL metrics may vary greatly from our current results if we were to perform the measurements in significantly more elastic or more viscous samples [37], at a different excitation frequency range, or with a very different ROE (e.g., micrometer-scale ROE in PF-OCE [14] or nanobomb OCE [28]). The MSR metrics are also likely to be different in side-by-side samples with larger stiffness contrast, or in samples with finite inclusion size [30]. Modifications to any factors that influence the system

Biomedical Optics EXPRESS

responses and the elastogram at any stage of the elastography workflow (Fig. 1) could in principle produce results that are inconsistent with those presented in this paper.

7. Conclusion

We presented a dynamic ARF-OCE experimental investigation of the conjecture that in order to obtain an elastogram with high spatial resolution, the applied mechanical excitation must be spatially localized to a small region in the sample such that the response it produces is also confined to a smaller spatial range. Our experimental designs were built upon our previous studies [29] and a generalized framework (that expands upon the framework in Hepburn et al. [30]) for understanding the factors that influence the quality of the elastogram at different stages of the elastography workflow. First, in Experiment 1, we found that localized excitation with a smaller ROE produced a displacement response with smaller ROR in the sample, but this trend was a function of the mechanical properties of the sample. Second, in Experiment 2, we found that localized ARF excitation with a smaller ROE resulted in higher quality strain elastograms, i.e., with superior spatial resolution, contrast, and CNR compared to a larger ROE. Although superior spatial resolution was obtained from wide-area excitation in our experiments, contrast and CNR were degraded compared to both localized excitation geometries. Lastly, comparing the ROR and elastogram quality characterized in Experiments 1 and 2, respectively, we found that a smaller ROR was correlated to an improved elastogram quality, but this correlation was also affected by the mechanical properties of the sample. Therefore, our experimental results as a whole support the above conjecture, but further studies are required to comprehensively interpret the results from wide-area versus localized excitations. Beyond the conclusions that can be drawn from our experimental results for dynamic ARF-OCE, we believe that our elastography framework and experimental approach presented in this paper have the potential to provide a basis for quantitative analysis of elastogram quality in OCE that can be adapted in an application-specific manner to different OCE systems.

Funding

National Institute of Biomedical Imaging and Bioengineering (5R21EB022927, 5R21EB024747).

Acknowledgments

This work made use of the Cornell Center for Materials Research Facilities supported by the National Science Foundation under Award Number DMR-1719875. The authors thank Ms. Raisa B. Rasul for assisting with part of the ARF-OCE experiments.

Disclosures

The authors declare no conflicts of interest.

References

1. A. J. Engler, S. Sen, H. L. Sweeney, and D. E. Discher, "Matrix Elasticity Directs Stem Cell Lineage Specification," Cell **126**(4), 677–689 (2006).
2. T. Mammoto, A. Mammoto, and D. E. Ingber, "Mechanobiology and Developmental Control," Annu. Rev. Cell Dev. Biol. **29**(1), 27–61 (2013).
3. M. J. Paszek, N. Zahir, K. R. Johnson, J. N. Lakins, G. I. Rozenberg, A. Gefen, C. A. Reinhart-King, S. S. Margulies, M. Dembo, D. Boettiger, D. A. Hammer, and V. M. Weaver, "Tensional homeostasis and the malignant phenotype," Cancer Cell **8**(3), 241–254 (2005).
4. D. Wirtz, K. Konstantopoulos, and P. C. Searson, "The physics of cancer: the role of physical interactions and mechanical forces in metastasis," Nat. Rev. Cancer **11**(7), 512–522 (2011).
5. K. J. Glaser, A. Manduca, and R. L. Ehman, "Review of MR elastography applications and recent developments," J. Magn. Reson. Imaging **36**(4), 757–774 (2012).

Biomedical Optics EXPRESS

6. R. M. S. Sigrist, J. Liau, A. E. Kaffas, M. C. Chammas, and J. K. Willmann, "Ultrasound Elastography: Review of Techniques and Clinical Applications," Theranostics **7**(5), 1303–1329 (2017).
7. G. Coceano, M. S. Yousafzai, W. Ma, F. Ndoye, L. Venturelli, I. Hussain, S. Bonin, J. Niemela, G. Scoles, D. Cojoc, and E. Ferreri, "Investigation into local cell mechanics by atomic force microscopy mapping and optical tweezer vertical indentation," Nanotechnology **27**(6), 065102 (2016).
8. M. Keating, A. Kurup, M. Alvarez-Elizondo, A. J. Levine, and E. Botvinick, "Spatial distributions of pericellular stiffness in natural extracellular matrices are dependent on cell-mediated proteolysis and contractility," Acta Biomater. **57**, 304–312 (2017).
9. M. Radmacher, R. W. Tillamnn, M. Fritz, and H. E. Gaub, "From molecules to cells: imaging soft samples with the atomic force microscope," Science **257**(5078), 1900–1905 (1992).
10. J. A. Mulligan, G. R. Untracht, S. N. Chandrasekaran, C. N. Brown, and S. G. Adie, "Emerging Approaches for High-Resolution Imaging of Tissue Biomechanics With Optical Coherence Elastography," IEEE J. Sel. Top. Quantum Electron. **22**(3), 246–265 (2016).
11. B. F. Kennedy, P. Wijesinghe, and D. D. Sampson, "The emergence of optical elastography in biomedicine," Nat. Photonics **11**(4), 215–221 (2017).
12. K. V. Larin and D. D. Sampson, "Optical coherence elastography - OCT at work in tissue biomechanics," Biomed. Opt. Express **8**(2), 1172–1202 (2017).
13. K. M. Kennedy, L. Chin, R. A. McLaughlin, B. Latham, C. M. Saunders, D. D. Sampson, and B. F. Kennedy, "Quantitative micro-elastography: imaging of tissue elasticity using compression optical coherence elastography," Sci. Rep. **5**(1), 15538 (2015).
14. N. Leartprapun, R. R. Iyer, G. R. Untracht, J. A. Mulligan, and S. G. Adie, "Photonic force optical coherence elastography for three-dimensional mechanical microscopy," Nat. Commun. **9**(1), 2079 (2018).
15. X. Qian, T. Ma, M. Yu, X. Chen, K. K. Shung, and Q. Zhou, "Multi-functional Ultrasonic Micro-elastography Imaging System," Sci. Rep. **7**(1), 1230 (2017).
16. G. Scarcelli, W. J. Polacheck, H. T. Nia, K. Patel, A. J. Grodzinsky, R. D. Kamm, and S. H. Yun, "Noncontact three-dimensional mapping of intracellular hydromechanical properties by Brillouin microscopy," Nat. Methods **12**(12), 1132–1134 (2015).
17. M. Fatemi and J. F. Greenleaf, "Vibro-acoustography: An imaging modality based on ultrasound-stimulated acoustic emission," Proc. Natl. Acad. Sci. U. S. A. **96**(12), 6603–6608 (1999).
18. C. Shih, C. Huang, Q. Zhou, and K. K. Shung, "High-Resolution Acoustic-Radiation-Force-Impulse Imaging for Assessing Corneal Sclerosis," IEEE Trans. Med. Imaging **32**(7), 1316–1324 (2013).
19. J. J. Dahl, "Acoustic Radiation Force Imaging," in *Emerging Imaging Technology in Medicine*, M. A. Anastasio and P. La Riviere, eds. (CRC Press, 2013), pp. 201–220.
20. K. R. Nightingale, M. L. Palmeri, R. W. Nightingale, and G. E. Trahey, "On the feasibility of remote palpation using acoustic radiation force," J. Acoust. Soc. Am. **110**(1), 625–634 (2001).
21. R. E. Mahaffy, C. K. Shih, F. C. MacKintosh, and J. Käs, "Scanning Probe-Based Frequency-Dependent Microrheology of Polymer Gels and Biological Cells," Phys. Rev. Lett. **85**(4), 880–883 (2000).
22. M. Stolz, R. Raiteri, A. U. Daniels, M. R. VanLandingham, W. Baschong, and U. Aebi, "Dynamic Elastic Modulus of Porcine Articular Cartilage Determined at Two Different Levels of Tissue Organization by Indentation-Type Atomic Force Microscopy," Biophys. J. **86**(5), 3269–3283 (2004).
23. R. C. Paietta, S. E. Campbell, and V. L. Ferguson, "Influences of spherical tip radius, contact depth, and contact area on nanoindentation properties of bone," J. Biomech. **44**(2), 285–290 (2011).
24. D. Chavan, J. Mo, M. de Groot, A. Meijering, J. F. de Boer, and D. Iannuzzi, "Collecting optical coherence elastography depth profiles with a micromachined cantilever probe," Opt. Lett. **38**(9), 1476–1478 (2013).
25. L. Ambrozinski, S. Song, S. J. Yoon, I. Pelivanov, D. Li, L. Gao, T. T. Shen, R. K. Wang, and M. O'Donnell, "Acoustic micro-tapping for non-contact 4D imaging of tissue elasticity," Sci. Rep. **6**(1), 38967 (2016).
26. T. M. Nguyen, B. Arnal, S. Song, Z. Huang, R. K. Wang, and M. O'Donnell, "Shear wave elastography using amplitude-modulated acoustic radiation force and phase-sensitive optical coherence tomography," J. Biomed. Opt. **20**(1), 016001 (2015).
27. F. Zvietcovich, J. P. Rolland, J. Yao, P. Meemon, and K. J. Parker, "Comparative study of shear wave-based elastography techniques in optical coherence tomography," J. Biomed. Opt. **22**(3), 035010 (2017).
28. C. H. Liu, D. Nevozhay, A. Schill, M. Singh, S. Das, A. Nair, Z. Han, S. Aglyamov, K. V. Larin, and K. V. Sokolov, "Nanobomb optical coherence elastography," Opt. Lett. **43**(9), 2006–2009 (2018).
29. R. R. Iyer, N. Leartprapun, and S. G. Adie, *Design and characterization of a multimodal system for 3D structural and mechanical imaging (Conference Presentation)*, SPIE BiOS (SPIE, 2018), Vol. 10496.
30. M. S. Hepburn, P. Wijesinghe, L. Chin, and B. F. Kennedy, "Analysis of spatial resolution in phase-sensitive compression optical coherence elastography," Biomed. Opt. Express **10**(3), 1496–1513 (2019).
31. B. F. Kennedy, X. Liang, S. G. Adie, D. K. Gerstmann, B. C. Quirk, S. A. Boppart, and D. D. Sampson, "In vivo three-dimensional optical coherence elstography," Opt. Express **19**(7), 6623–6634 (2011).
32. B. F. Kennedy, R. A. McLaughlin, K. M. Kennedy, L. Chin, A. Curatolo, A. Tien, B. Latham, C. M. Saunders, and D. D. Sampson, "Optical coherence micro-elastography: mechanical-contrast imaging of tissue microstructure," Biomed. Opt. Express **5**(7), 2113–2124 (2014).

Biomedical Optics EXPRESS

33. W. Kim, V. L. Ferguson, M. Borden, and C. P. Neu, "Application of Elastography for the Noninvasive Assessment of Biomechanics in Engineered Biomaterials and Tissues," Ann. Biomed. Eng. **44**(3), 705–724 (2016).
34. S. G. Adie, X. Liang, B. F. Kennedy, R. John, D. D. Sampson, and S. A. Boppart, "Spectroscopic optical coherence elastography," Opt. Express **18**(25), 25519–25534 (2010).
35. Z. Han, M. Singh, S. R. Aglyamov, C. H. Liu, A. Nair, R. Raghunathan, C. Wu, J. Li, and K. V. Larin, "Quantifying tissue viscoelasticity using optical coherence elastography and the Rayleigh wave model," J. Biomed. Opt. **21**(9), 090504 (2016).
36. S. Wang and K. V. Larin, "Noncontact depth-resolved micro-scale optical coherence elastography of the cornea," Biomed. Opt. Express **5**(11), 3807–3821 (2014).
37. N. Leartprapun, R. R. Iyer, and S. G. Adie, "Model-independent quantification of soft tissue viscoelasticity with dynamic optical coherence elastography," Proc. SPIE **10053**, 1005322 (2017).
38. V. Crecea, A. Ahmad, and S. A. Boppart, "Magnetomotive optical coherence elastography for microrheology of biological tissues," J. Biomed. Opt. **18**(12), 121504 (2013).
39. W. Qi, R. Li, T. Ma, K. Kirk Shung, Q. Zhou, and Z. Chen, "Confocal acoustic radiation force optical coherence elastography using a ring ultrasonic transducer," Appl. Phys. Lett. **104**(12), 123702 (2014).
40. F. Zvietcovich, J. P. Rolland, and K. J. Parker, "An approach to viscoelastic characterization of dispersive media by inversion of a general wave propagation model," J. Innovative Opt. Health Sci. **10**(06), 1742008 (2017).
41. E. W. Chang, J. B. Kobler, and S. H. Yun, "Subnanometer optical coherence tomographic vibrography," Opt. Lett. **37**(17), 3678–3680 (2012).
42. W. M. Allen, K. M. Kennedy, Q. Fang, L. Chin, A. Curatolo, L. Watts, R. Zilkens, S. L. Chin, B. F. Dessauvagie, B. Latham, C. M. Saunders, and B. F. Kennedy, "Wide-field quantitative micro-elastography of human breast tissue," Biomed. Opt. Express **9**(3), 1082–1096 (2018).
43. J. M. Carcione, "Chapter 5 - The Reciprocity Principle," in *Wave Fields in Real Media (Third Edition)* (Elsevier, 2015), pp. 231–246.
44. P. J. Hollender, S. J. Rosenzweig, K. R. Nightingale, and G. E. Trahey, "Single- and multiple-track-location shear wave and acoustic radiation force impulse imaging: matched comparison of contrast, contrast-to-noise ratio and resolution," Ultrasound Med. Biol. **41**(4), 1043–1057 (2015).
45. F. Kallel, M. Bertrand, and J. Ophir, "Fundamental limitations on the contrast-transfer efficiency in elastography: An analytic study," Ultrasound Med. Biol. **22**(4), 463–470 (1996).
46. T. Varghese and J. Ophir, "An analysis of elastographic contrast-to-noise ratio," Ultrasound Med. Biol. **24**(6), 915–924 (1998).
47. K. M. Kennedy, C. Ford, B. F. Kennedy, M. B. Bush, and D. D. Sampson, "Analysis of mechanical contrast in optical coherence elastography," J. Biomed. Opt. **18**(12), 121508 (2013).
48. J. Jang and J. H. Chang, "Design and Fabrication of Double-Focused Ultrasound Transducers to Achieve Tight Focusing," Sensors **16**(8), 1248 (2016).
49. L. Gao, K. J. Parker, S. K. Alam, and R. M. Lerner, "Sonoelasticity imaging: Theory and experimental verification," J. Acoust. Soc. Am. **97**(6), 3875–3886 (1995).
50. E. L. Madsen, M. A. Hobson, H. Shi, T. Varghese, and G. R. Frank, "Tissue-mimicking agar/gelatin materials for use in heterogeneous elastography phantoms," Phys. Med. Biol. **50**(23), 5597–5618 (2005).
51. E. L. Baker, J. Lu, D. Yu, R. T. Bonnecaze, and M. H. Zaman, "Cancer cell stiffness: integrated roles of three-dimensional matrix stiffness and transforming potential," Biophys. J. **99**(7), 2048–2057 (2010).
52. J. M. Barnes, L. Przybyla, and V. M. Weaver, "Tissue mechanics regulate brain development, homeostasis and disease," J. Cell Sci. **130**(1), 71–82 (2017).
53. J. Fenner, A. C. Stacer, F. Winterroth, T. D. Johnson, K. E. Luker, and G. D. Luker, "Macroscopic stiffness of breast tumors predicts metastasis," Sci. Rep. **4**(1), 5512 (2015).
54. B. H. Park, M. C. Pierce, B. Cense, S. H. Yun, M. Mujat, G. J. Tearney, B. E. Bouma, and J. F. de Boer, "Real-time fiber-based multi-functional spectral-domain optical coherence tomography at 1.3 um," Opt. Express **13**(11), 3931–3944 (2005).
55. K. J. Parker and N. Baddour, "The Gaussian shear wave in a dispersive medium," Ultrasound Med. Biol. **40**(4), 675–684 (2014).
56. L. Chin, A. Curatolo, B. F. Kennedy, B. J. Doyle, P. R. T. Munro, R. A. McLaughlin, and D. D. Sampson, "Analysis of image formation in optical coherence elastography using a multiphysics approach," Biomed. Opt. Express **5**(9), 2913–2930 (2014).
57. G. Guan, C. Li, Y. Ling, Y. Yang, J. B. Vorstius, R. P. Keatch, R. W. Wang, and Z. Huang, "Quantitative evaluation of degenerated tendon model using combined optical coherence elastography and acoustic radiation force method," J. Biomed. Opt. **18**(11), 111417 (2013).
58. C. Li, G. Guan, Y. Ling, Y. T. Hsu, S. Song, J. T. J. Huang, S. Lang, R. K. Wang, Z. Huang, and G. Nabi, "Detection and characterisation of biopsy tissue using quantitative optical coherence elastography (OCE) in men with suspected prostate cancer," Cancer Lett. **357**(1), 121–128 (2015).
59. N. C. Rouze, Y. Deng, C. A. Trutna, M. L. Palmeri, and K. R. Nightingale, "Characterization of Viscoelastic Materials Using Group Shear Wave Speeds," IEEE Trans. Ultrason., Ferroelect., Freq. Contr. **65**(5), 780–794 (2018).
60. S. Beke, B. Farkas, I. Romano, and F. Brandi, "3D scaffold fabrication by mask projection excimer laser stereolithography," Opt. Mater. Express **4**(10), 2032 (2014).

Biomedical Optics EXPRESS

61. R. Sunyer, A. J. Jin, R. Nossal, and D. L. Sackett, "Fabrication of hydrogels with steep stiffness gradients for studying cell mechanical response," PLoS One **7**(10), e46107 (2012).
62. C. Sun, B. A. Standish, B. Vuong, X. Y. Wen, and V. X. D. Yang, "Digital image correlation–based optical coherence elastography," J. Biomed. Opt. **18**(12), 121515 (2013).
63. K. Kurokawa, S. Makita, Y. Hong, and Y. Yasuno, "Two-dimensional micro-displacement measurement for laser coagulation using optical coherence tomography," Biomed. Opt. Express **6**(1), 170–190 (2015).
64. J. Fu, M. Haghighi-Abayneh, F. Pierron, and P. D. Ruiz, "Depth-Resolved Full-Field Measurement of Corneal Deformation by Optical Coherence Tomography and Digital Volume Correlation," Exp. Mech. **56**(7), 1203–1217 (2016).
65. H. Spahr, C. Pfäffle, P. Koch, H. Sudkamp, G. Hüttmann, and D. Hillmann, "Interferometric detection of 3D motion using computational subapertures in optical coherence tomography," Opt. Express **26**(15), 18803–18816 (2018).
66. M. M. Nguyen, S. Zhou, J. Robert, V. Shamdasani, and H. Xie, "Development of Oil-in-Gelatin Phantoms for Viscoelasticity Measurement in Ultrasound Shear Wave Elastography," Ultrasound Med. Biol. **40**(1), 168–176 (2014).